

Banana Split: Improved Cosmological Constraints with Two Light-Curve-Shape and Color Populations Using Union3.1+UNITY1.8

DAVID RUBIN,^{1,2} TAYLOR HOYT,² GREG ALDERING,² AND SAUL PERLMUTTER^{2,3}

¹*Department of Physics and Astronomy, University of Hawai‘i at Mānoa, Honolulu, Hawai‘i 96822*

²*Physics Division, E.O. Lawrence Berkeley National Laboratory, 1 Cyclotron Rd., Berkeley, CA, 94720, USA*

³*Department of Physics, University of California Berkeley, Berkeley, CA 94720, USA*

ABSTRACT

SNe Ia have been used to provide key constraints on the equation-of-state parameter of dark energy. They are generally standardized under the assumption that they belong to a single population, with luminosities standardized in a continuous (roughly linear) fashion using the observed light-curve timescale. We update the Union3+UNITY1.5 SN cosmology analysis in light of increasing evidence for at least two core populations of SNe Ia and apply this “UNITY1.8” model to the updated “Union3.1” compilation (Hoyt et al. 2026). In addition to finding evidence for two different light-curve-shape (x_1) distributions, we also find that the color distributions are different, that the light-curve-shape/magnitude standardization relations are different, and that these populations have different distributions across host-galaxy stellar mass and redshift. Importantly, we find that the residual host-mass luminosity step found in prior SN Ia cosmology analyses is now consistent with zero for unreddened SNe. We report a significantly tightened constraint on the split in the red-color standardization between SNe in low- and high-mass galaxies. We find that the estimated uncertainties shrink on cosmological parameters when fitting the same SNe assuming two modes versus one mode. We confirm similar trends in simulated data when running both versions of UNITY on the same (two-mode) simulations. For a flat Λ CDM cosmology, we find $\Omega_m = 0.334^{+0.025}_{-0.024}$ from SNe alone; for a flat w_0 - w_a cosmology, we find $w_0 = -0.760^{+0.084}_{-0.082}$ and $w_a = -0.79^{+0.28}_{-0.30}$ when including SNe, BAO, and CMB. In the 2D w_0 - w_a plane, adding SNe to BAO and compressed CMB increases the tension with flat Λ CDM from 2.1σ to 2.6σ .

Keywords: Cosmology, Supernovae

1. INTRODUCTION

For the first time since the discovery of the accelerated expansion of the universe (Riess et al. 1998; Perlmutter et al. 1999), the redshift dependence of the dark energy equation of state parameter (w) seems to be in ~ 3 – 4σ tension with that of a cosmological constant (i.e., $w = -1$ for all time). This was shown at $\sim 2\sigma$ significance in Rubin et al. (2025) who combined Union3 SNe with Planck CMB and 6dF+SDSS+BOSS+eBOSS BAO (Planck Collaboration et al. 2020; Beutler et al. 2011; Ross et al. 2015; Alam et al. 2017; du Mas des Bourboux et al. 2020; Neveux et al. 2020; Bautista et al. 2021; Raichoor et al. 2021; Hou et al. 2021; de Mattia et al. 2021). The statistical significance increased to 4.2σ after combining the Dark Energy Survey (DES) SN Year 5 results (DES Collaboration et al. 2024) with the Dark Energy Spectroscopic Instrument (DESI) collaboration Baryon Acoustic Oscillation (BAO) measure-

ments (Adame et al. 2025; DESI Collaboration et al. 2025). That statistical significance decreased with a re-calibration (and bug fix) of the DES Year 5 results, but remains at 3.2σ for DES+CMB+DESI (Popovic et al. 2025a,b).

Since the publication of the Union3 SN Ia cosmology analysis, a few developments and improvements motivated us to update its underlying cosmological framework (Unified Nonlinear Inference for Type Ia cosmologY, UNITY, Rubin et al. 2015, 2025) and the supporting data. First, as previously mentioned, the DESI BAO results supersede the earlier SDSS+BOSS+eBOSS (Alam et al. 2017, 2021) measurements used in Union3.¹ Second, a growing body of evidence suggests that stan-

¹ Union3 also used BAO from 6dF (Beutler et al. 2011) which is mostly independent of DESI and thus should not be replaced.

dardizing SNe Ia using their light-curve widths is more complex than the simple linear standardization historically used and also used in Union3 (Burns et al. 2014; Wojtak et al. 2023; Garnavich et al. 2023; Ginolini et al. 2025a; Wojtak & Hjorth 2025). Third, the correlation of host-galaxy properties with SN Ia characteristics has emerged as a significant, underreported systematic discrepancy between independent analyses of the same SNe, thereby also impacting the combined interpretation of BAO and CMB with SNe (Efstathiou 2025; Hoyt et al. 2025; Vincenzi et al. 2025).

This paper is organized as follows. Section 2 details the updates implemented in UNITY since Rubin et al. (2025) (“UNITY1.7”). Section 3 outlines the evidence for two light-curve-shape modes and updates UNITY1.7 to fit for this (“UNITY1.8”). Section 3 also validates our updates against both real and simulated data. Section 4 shows the results for SN standardization from applying UNITY1.8 to Union3.1. Section 5 shows our Union3.1+UNITY1.8 cosmological constraints with and without external probes. Finally Section 6 summarizes and concludes.

2. UNITY1.7: IMPROVEMENTS SINCE UNITY1.5

2.1. UNITY1.5 *Review*

The Unified Nonlinear Inference for Type Ia cosmologY framework (UNITY) is a Bayesian hierarchical model for computing SN cosmological constraints. It simultaneously models SN standardization, light-curve-shape and color population distributions, outliers, unexplained dispersion, selection effects, systematic uncertainties, and cosmological parameters. The underlying approach (described and motivated in more detail in Rubin et al. 2015, 2025) is to describe SN cosmology as a regression problem where the results of light-curve fits can be forward modeled in an analysis that treats all parameters simultaneously. When there is ambiguity about the correct model in way that affects the cosmological results (for example, whether the host-galaxy relations should evolve with redshift), UNITY parameterizes and marginalizes out these choices.

To review, the UNITY1.5 standardization equation (Equation 5 from Rubin et al. 2025) models the rest-frame B -band magnitude (m_B) for each SN as:

$$\begin{aligned} m_B^{\text{model}} = & M_B + \mu(z, \text{ cosmology}) \\ & - \alpha x_1^{\text{true}} + \beta_B c_B^{\text{true}} \\ & + [\beta_R^{\text{low}} (1 - P_{\text{eff}}^{\text{high}}) + \beta_R^{\text{high}} P_{\text{eff}}^{\text{high}}] c_R^{\text{true}} \\ & - \delta(z = 0) P_{\text{eff}}^{\text{high}}. \end{aligned} \quad (1)$$

M_B is the rest-frame B -band absolute magnitude, μ is the distance modulus, α is the x_1 standardization co-

efficient, β_B is the color standardization coefficient for Gaussian core of the color distribution, β_R^{low} and β_R^{high} are the color standardization coefficient of the red exponential tail in low-mass and high-mass hosts respectively, and $\delta(z = 0)$ is the host-mass standardization coefficient at low redshift. $P_{\text{eff}}^{\text{high}}$ is the probability of a host-galaxy behaving like a low-redshift host galaxy having high stellar mass:

$$\begin{aligned} P_{\text{eff}}^{\text{high}} \equiv & P^{\text{high}} \left[\frac{1.9}{0.9 \cdot 10^{0.95} z + 1} \left[1 - \frac{\delta(z = \infty)}{\delta(z = 0)} \right] \right. \\ & \left. + \frac{\delta(z = \infty)}{\delta(z = 0)} \right]; \end{aligned} \quad (2)$$

the functional form of the redshift dependence is motivated in Rigault et al. (2013) and is also similar to the curve in Figure 9 of Childress et al. (2014). P^{high} was computed assuming Gaussian stellar-mass uncertainties and a low/high-stellar-mass cutoff of $10^{10} M_\odot$.

There are three latent per-SN parameters (x_1^{true} , c_B^{true} , and c_R^{true}) that are explicitly marginalized over (as opposed to analytically marginalized over) for every SN in the analysis, and these parameters have population-distribution priors with their own parameters (“hyperparameters”). The x_1 distribution is modeled as an exponentially modified Gaussian distribution:

$$x_1^{\text{true}} \sim \text{ExpModNormal}(x_1^*, R_{x_1}^2, 1/\tau_{x_1}). \quad (3)$$

The red colors c_R^{true} are assumed to be distributed as an exponential while the blue colors c_B^{true} are assumed to be Gaussian distributed:

$$c_R^{\text{true}} \sim \text{Exp}(1/\tau_{c_R}) \quad (4)$$

$$c_B^{\text{true}} \sim \mathcal{N}(c_B^*, R_c^2). \quad (5)$$

Each of these hyperparameters above really consists of six numbers, as each is allowed to vary independently in bins of low/high host-galaxy stellar mass and low/mid/high redshift. The motivation for the two sources of color variation is intrinsic (c_B) and extinction (c_R), although UNITY is an empirical model and this correspondence does not have to be exact. Of course, if the c_R^{true} values really do have a good correspondence with extinction, the distribution will likely be more sharply peaked than an exponential (Hatano et al.

1998; Hallgren et al. 2025); we validate our assumptions against the data in Section 3.4.^{2,3}

The model for x_1 is simply

$$x_1^{\text{model}} = x_1^{\text{true}} \quad (6)$$

for each SN and the model for c is

$$c^{\text{model}} = c_B^{\text{true}} + c_R^{\text{true}} \quad (7)$$

for each SN. The observed $\{m_B^{\text{obs}}, x_1^{\text{obs}}, c^{\text{obs}}\}$ is compared to the model $\{m_B^{\text{model}}, x_1^{\text{model}}, c^{\text{model}}\}$ assuming multi-dimensional (correlated) Gaussian uncertainties (including unexplained dispersion in m_B , x_1 , and c) modified with a model of the selection effects (Rubin et al. 2015 Appendix B). The inlier distribution is mixed with an outlier distribution which is also assumed to be Gaussian (but is constrained to be broader to capture any SNe not well modeled by the inlier distribution).

2.2. UNITY Updates

This update paper provides an opportunity to make some smaller, technical tweaks to UNITY. The current best version, referred to as UNITY1.5, was developed for the Union3 analysis (Rubin et al. 2025) and we begin our updates from the version with the corrected parameter limit for the width of the outlier distribution in

² We also perform a toy-model test where we generate some fraction of the SN population at zero extinction and the rest with an exponential distribution. This extinction is convolved with a Gaussian intrinsic color distribution and Gaussian uncertainties to get the observed color distribution. We cut at an observed color of 0.3, as we do for the real data. When fitting with our Gaussian c_B^{true} /exponential c_R^{true} model, we find a bias in the recovered mean distance modulus of 0.0016 magnitudes per percent of SNe in the zero-extinction spike. This bias is generally small compared to other uncertainties and would partially cancel in redshift if similar fractions were in the spike as a function of redshift. Models that do a better job modeling intrinsic and extrinsic color at the light-curve-fitting stage are an important area of ongoing research (Mandel et al. 2022; Hand et al. 2025; Kenworthy et al. 2025).

³ Note that some models allow for the opposite: a two-tailed extinction distribution, where the modal extinction is greater than zero (Wojtak et al. 2023). One practical difficulty with this is that a two-tailed extinction distribution can be similar to a Gaussian-convolved exponential, which would make it difficult to assign the c_B (Gaussian distributed) and c_R (extinction-like, here assumed exponentially distributed) colors; one can see this in the Wojtak et al. (2023) model in the degeneracy between the mean intrinsic color and the degree that the extinction distribution is two-tailed. Another factor is that, for some of the Wojtak et al. (2023) models, there is no unexplained dispersion other than the dispersion in extinction R_B , which may favor a two-tailed distribution so that all SNe have some extinction (and thus some unexplained dispersion). Note that there is no unexplained dispersion in color for any of the Wojtak et al. (2023) models. In any case, Wojtak et al. (2023) finds $\lesssim 3$ -to-1 posterior density in favor of a two-tailed distribution (depending on SN sample) so we assume exponentially distributed c_R for now.

exponentially distributed latent color ($\sigma_{c_R}^{\text{outl}}$, we refer to the corrected version as “UNITY1.6”). Table 1 outlines the versions of UNITY referenced and developed in this paper.

UNITY1.7 now fits the mass of the host-mass step instead of fixing it to $10^{10} M_{\odot}$. This mass affects both the luminosity step $\delta(z = 0)$ and the β_R step (in other words, the difference of β_R with host-galaxy stellar mass, $\beta_R^{\text{low}} - \beta_R^{\text{high}}$); see Equation 1. Differences in the galaxy photometry and underlying galaxy SED model can lead to systematic offsets in estimates of galaxy stellar mass as large as 0.5 dex, so even if one knew *a priori* that the step was at $10^{10} M_{\odot}$ (as was assumed in UNITY1.5 and many prior analyses), the apparent location could be different, making it an important value to solve for. Including it as a fit parameter naturally propagates the corresponding uncertainties into the other parameters. See Hoyt et al. (2026) for a more detailed discussion.

UNITY now supports distance-ladder constraints by replacing the cosmological integral with a distance modulus from another measurement (e.g., from Cepheids or Tip of the Red-Giant Branch). These distances will have their own distance-modulus covariance matrix from the lower rungs of the distance ladder (e.g., Riess et al. 2022 Figure 11), and UNITY can now include this covariance matrix. UNITY can also include unexplained dispersion from the lower rungs, in case the calibrators have distance-modulus dispersion larger than their uncertainties. Making full use of this capability on real data requires collecting light curves for many calibrator SNe which are which are not in Union3, so we pursue this in an upcoming H_0 paper (Union3.2, Hoyt et al. in prep.).

We also made a mild UNITY update to the generation of the distance moduli. As part of its set of parameters, UNITY infers a distance-modulus $\mu(z)$ function. This function is either a parameterized cosmological model (e.g., flat Λ CDM) or is constructed from a set of distance moduli. As discussed in Section 5.1, the set of distance moduli is parameterized by adding the distance modulus of a flat Λ CDM model with $\Omega_m = 0.3$ and spline-interpolated values as a function of redshift. However, when not including a distance ladder, there is a degeneracy between adding a constant to all distance moduli and adjusting \mathcal{M}_B . In UNITY1.5, this degeneracy was broken by adding a virtual spline node at $z = 0$ and fixing this node to 0. In the UNITY versions presented here, we instead fix this node to $-(\text{the sum of all other nodes})$. This is more effective at breaking the degeneracy, so there is less covariance between the quoted distance moduli. This covariance does not have

Table 1. Table comparing recent UNITY versions.

UNITY Version	Reference	Summary
1.5	Rubin et al. (2025)	Used for Union3 analysis. Models one inlier population of SNe with Gaussian * exponential x_1 and c populations.
1.6	Rubin et al. (2025)	Same as UNITY1.5 above, but with improved c_R^{true} outlier parameter limit discussed in Rubin et al. (2025) Appendix B.
1.7	This work and Hoyt et al. (2026)	Also includes fit for mass-step location and distance-ladder capability.
1.8	This work	Union3.1 model that includes two separate SN populations with different (Gaussian) x_1^{true} and c_B^{true} populations, different α values, and extra unexplained dispersion for the faster population.

an impact on the cosmological constraints, so this is a cosmetic improvement.

As mentioned in the Introduction, we also update some of the external cosmological constraints. We replace the SDSS+BOSS+eBOSS Baryon Acoustic Oscillation (BAO) measurements with DESI DR2 distances (DESI Collaboration et al. 2025) which are higher precision over the same sky. However, we keep 6dF (Beutler et al. 2011), which has little sky overlap with DESI. Planck CMB (Planck Collaboration et al. 2020) and Big Bang nucleosynthesis (Cooke et al. 2016) constraints carry over from Union3.⁴

We also update the Cepheid-based Hubble constant measurement to the latest from SH0ES (73.17 ± 0.86 km/s/Mpc, Breuval et al. 2024), and we update the TRGB measurement to the latest from CCHP (70.39 ± 1.80 km/s/Mpc, Freedman et al. 2025). Of course, applying these measurements as priors in the analysis ignores the covariance between H_0 and other cosmological parameters; as mentioned above, we will explore this in a subsequent paper that correctly incorporates the lower rungs of the distance ladder into UNITY (Hoyt et al. in prep.). Nevertheless, it gives an approximate sense of how the cosmological constraints are affected by external Hubble-constant measurements of different values and precisions.

3. UNITY1.8: STANDARDIZATION WITH MULTIPLE POPULATIONS

This Section describes the evidence for multiple populations of SNe Ia (Section 3.1) and the updates to UNITY that we make (Section 3.2). All of these UNITY changes were made with the cosmology hidden (a “blinded” analysis, Maccoun & Perlmutter 2015) until after the analysis had been validated on simulated

data (Section 3.3) and by examining the predictive posterior distributions (Section 3.4). We revisit alternate models as part of the pre-unblinding tests described in Section 3.5.

3.1. Motivation

A key component in the empirical standardization of SNe Ia is the light curve shape, as parameterized by its rate of decline after maximum (β in Pskovskii 1977, Δm_{15} in Phillips 1993; Tripp 1997, 1998), light-curve width “stretch” (Perlmutter et al. 1997b,a), or a light-curve-shape template parameter (Δ in Riess et al. 1996 or x_1 in Guy et al. 2007). In the canonical single-degenerate SNe Ia progenitor model—where a WD accretes matter from a donor star until it reaches the Chandrasekhar mass, at which point a thermonuclear runaway is triggered—the rise time of the light curve is ostensibly proportional to the amount of radioactive ^{56}Ni generated (Arnett 1982; Arnett et al. 1985; Pinto & Eastman 2000). However, when broadening the SNe Ia progenitor landscape to include WD mergers, the light-curve width reflects a combination of the ejecta mass and the amount of ^{56}Ni (Scalzo et al. 2014). Thus, the Δm_{15} and x_1 parameters may be trying to account for two physical effects at once—much as the SALT c parameter tries to account simultaneously for both intrinsic color-luminosity correlations and reddening by line-of-sight dust. Here we briefly review evidence for non-linear and multi-mode models for the light-curve-shape standardization, then use that information to develop a suitable model for UNITY.

There has long been evidence that standardization is not a simple linear relation with light-curve shape. If nothing else, x_1 is commonly substituted for the Δm_{15} in the original Tripp (1998) linear-standardization relation, yet the relationship between these two light-curve-shape parameters is itself nonlinear (Guy et al. 2007; Kessler et al. 2009), so they cannot both be optimally

⁴ We also consider some newer approaches to modeling the Planck data and their impact on cosmology in subsection 5.2.

treated with linear standardization. Indeed, Phillips et al. (1999); Wang et al. (2006); Amanullah et al. (2010); Sullivan et al. (2010); Scolnic et al. (2014); Rubin et al. (2015); Burns et al. (2018); Garnavich et al. (2023); Ginolini et al. (2025b) show evidence for nonlinear standardization relations. Even so, merely expanding to a nonlinear standardization with respect to x_1 assumes a single unique mapping between SN Ia luminosity and x_1 . This does not have to be the case if, for example, there are multiple subpopulations, each with their own relation.

The evidence for discontinuous or multi-modal luminosity standardization at a given x_1 is growing. The x_1 distribution changes across host-galaxy types (Hamuy et al. 2000; Howell 2001; Sullivan et al. 2006; Smith et al. 2020; Wiseman et al. 2021; Garnavich et al. 2023; Larson et al. 2024; Senzel et al. 2025), with fast decliners more preferentially located in passive galaxies and slow decliners preferentially located in star-forming galaxies. As the mix of host-galaxy types changes with redshift, the x_1 distribution is thus expected to change too. Indeed, Nicolas et al. (2021) find that the x_1 is better described by two Gaussian modes than with a skewed Gaussian, and that the relative strengths of the modes evolves with redshift. Rigault et al. (2013) suggested a bimodality to Hubble residuals, with the second mode showing up only in passive host environments. Wojtak et al. (2023) incorporated this into their standardization model, having two subpopulations—“fast” and “slow” decliners—described by Gaussian distributions in x_1 . They found similar standardization luminosities, significantly different mean colors and reddening distributions, but found consistent luminosity-width slopes (α). They discussed a possible young vs. old interpretation of the two modes and expanded on it in Wojtak & Hjorth (2025).

Apart from indirect evidence related to different delay-time distributions, there are some more direct clues to the differences in the progenitor systems. Maguire et al. (2013) finds time-varying, blueshifted Na I D absorption in SNe only hosted by late-type galaxies, possibly indicating that these are single-degenerate systems that have undergone mass loss. Tucker (2025) finds that bimodal nebular phase emission, a sign of WD mergers, only occurs in passive galaxies. If SNe in old and young environments arise from different progenitor channels, there is no expectation that the population distributions, luminosity distribution, or standardization relations will be the same.

3.2. Defining the new standardization model

We therefore construct a two-mode UNITY model which we refer to as “UNITY1.8.” It includes sepa-

rate x_1 mean and dispersion (x_1^* and R^{x_1}) parameters for each of two modes, separate mean and dispersion of the blue-color (c^* and R^c) parameters, separate α values, separate absolute magnitudes (M_B), and separate unexplained dispersions. We investigated allowing β_B or β_R to be different between modes, but found almost identical β_B values and that β_R seems to correlate more with host-galaxy stellar mass (as in the UNITY1.5 model), so we do not include these splits as part of our nominal model. As with UNITY1.5, we split the red-color-population scale length (τ_{c_R}) in bins of both host-galaxy stellar mass and redshift, helping to lessen any biases if the extinction distribution changes with these parameters. We treat the blue-color population and x_1 distributions as associated with the modes, and so these do not get different values depending on redshift and host mass. However, the relative fractions of the modes are allowed to vary with both host-galaxy stellar mass and redshift.

In equation form, we update the UNITY1.5 standardization equation (Equation 5 of Rubin et al. 2025, reproduced in Equation 1) to read:

$$\begin{aligned} & m_B^{\text{model, fast or slow}} \quad (8) \\ & = -\alpha^{\text{fast or slow}} \left(x_1^{\text{true}} - x_1^{*, \text{ fast or slow}} \right) \\ & + \beta_B c_B^{\text{true}} \\ & + [\beta_R^{\text{low}} (1 - P_{\text{eff}}^{\text{high}}) + \beta_R^{\text{high}} P_{\text{eff}}^{\text{high}}] c_R^{\text{true}} \\ & - \delta(z = 0) P_{\text{eff}}^{\text{high}} \\ & + M_B^{\text{fast or slow}} + \mu(\{z, \text{cosmology}\} \text{ or calibrator}) , \end{aligned}$$

where “fast” and “slow” refer to the lower- and higher- x_1 population, respectively. These are combined in a mixture model (along with the outlier distribution) so each SN is only probabilistically assigned into each population’s mode. Each x_1 mode is modeled as Gaussian:

$$x_1^{\text{true}} \sim \mathcal{N}(x_1^{*, \text{ fast or slow}}, (R_{x_1}^{\text{fast or slow}})^2) . \quad (9)$$

As in UNITY1.5, the red colors c_R^{true} are assumed to be distributed as an exponential while the blue colors c_B^{true} are assumed to be Gaussian distributed:

$$c_R^{\text{true}} \sim \text{Exp}(1/\tau_{c_R}) \quad (10)$$

$$c_B^{\text{true}} \sim \mathcal{N}(c_B^{*, \text{ fast or slow}}, (R_c^{\text{fast or slow}})^2) . \quad (11)$$

We present a detailed discussion of our SN results in Section 4, but Figure 1 illustrates our two-mode x_1 and c model, with the lower- x_1 mode showing up at higher host stellar mass and lower redshift (older populations, on average).

To summarize, unlike models that split samples on the *observed* value of x_1^{obs} , in this case x_1 influences

the relative probability of being in the fast or slow decliner subpopulations (with the subpopulations based on the preceding equations). When the standardizations are different for the two subpopulations, this has the interesting feature that a unique value of x_1 predicts two alternative standardization corrections (in some proportion). This uncertainty may explain part of the so-called “unexplained dispersion” encountered when attempting to standardize SNe Ia using light curve shape and color alone, but our simulated-data testing (Section 3.3) shows that UNITY1.7’s single-population model does not increase the unexplained dispersion much over UNITY1.8’s two-population model.

3.3. Simulated-Data Testing

Simulated-data testing is an essential part of a complex analysis to ensure the correctness of the results. We performed our simulated-data testing and validation before unblinding the cosmology results for real data. Our simulated-data testing is based on that done for Union3+UNITY1.5 (Rubin et al. 2025), updated to be based the new two-mode UNITY1.8 model. Detailed results are provided in Appendix A. Note we do not simulate from the UNITY model itself, but instead construct an independent simulation. This provides a more realistic (and more difficult) test for UNITY to pass than if the test data were simulated from UNITY and fed right back into it.

We ran 100 realizations of simulated data (each one with four simulated datasets) based on the UNITY1.8 model with two populations in x_1 . For each realization, we ran four UNITY variants: UNITY1.8 and 1.7 with flat Λ CDM and flat w_0-w_a (with Ω_m fixed so that external data need not be included). For each UNITY run, we used four chains with 2500 samples/chain, and (to be conservative) discarded the first half of each chain. This is sufficient sampling such that sampling errors on parameter estimates fell more than an order of magnitude below the typical uncertainty ($N_{\text{eff}} \sim 1000$). We restarted runs that got stuck or that did not sample well.

We summarize here key findings from the simulated-data testing, with more details provided in Appendix B.

1. The testing shows little evidence of bias ($\lesssim 0.2\sigma \pm 0.1\sigma$) in the inference of final cosmological parameters (H_0 , Ω_m , w_0 , w_a) using the nominal UNITY1.8 model, indicating our cosmological parameter inference from the real data is likely also minimally biased.
2. However, the cosmological-parameter inference is noticeably biased in the previous, single-mode- x_1

model (UNITY1.7) when fitting these two-mode simulations, with this bias ranging from 0.7σ on Ω_m to $0.3\text{--}0.5\sigma$ on the dark energy equation-of-state parameters.

3. UNITY1.8 estimates slightly smaller cosmological-parameter uncertainties when run on the same input simulated data. Note that the input simulations are based on a two-mode model.
4. Both UNITY1.7 and UNITY1.8 misestimate the outlier fraction present in the simulations, indicating that the outlier model needs more fidelity to match the data. This was also seen in Union3 (Rubin et al. 2025) and is generally not a cause for concern for two reasons. 1) There is very little covariance between the outlier-distribution parameters and the cosmological parameters. 2) Because the inlier distribution(s) are much narrower than the outlier distribution, the normalization of the outlier distribution does not strongly affect which SNe are recognized as outliers.
5. A non-zero correlation of SN luminosity with host mass δ_0 is introduced when attempting to model a two-mode population with UNITY1.7, suggesting at least part of the signal for the characteristic host-mass step seen in SN luminosities is a result of incomplete modeling of SN population diversity along the light-curve-shape axis.
6. The unexplained-dispersion values are biased somewhat high for UNITY1.7 and somewhat low for UNITY1.8. This bias is detectable using the aggregated 100 realizations, but is mild in any one realization. The fact that the bias is not large for UNITY1.7 (when fitting data generated with a two-mode model) implies that not much of the UNITY1.7 unexplained dispersion is due to the ambiguity over which mode a given SN is in and this likely carries over to the real data.
7. The absolute value of α is biased low by about 1.3σ in either cosmology considered, while the difference $\alpha^{\text{fast}} - \alpha^{\text{slow}}$ exhibits negligible bias ($< 0.1\sigma$). Thus, the evidence UNITY finds for a difference in α between the two x_1 populations is very likely real and not very biased in size. Other x_1 -related parameters are also biased, especially for the fast mode. A similar (but smaller) bias on standardization coefficients was seen by Rubin et al. (2025). These biases are generally small in absolute terms (e.g., population parameters biased by about 0.1 in x_1) and are thus difficult to diagnose. As

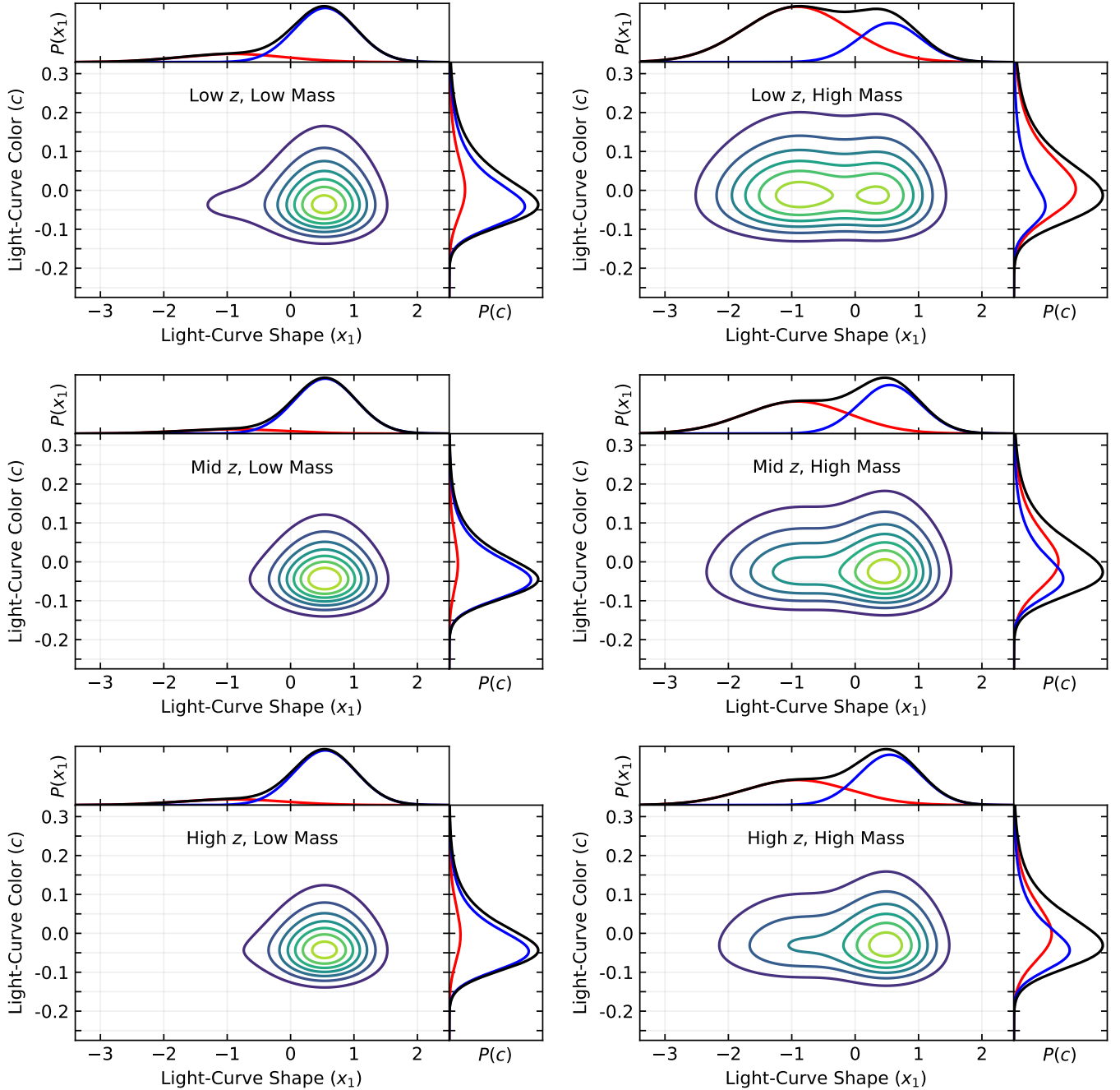


Figure 1. Two-mode population models from Union3.1+UNITY1.8. The x_1 and c_B distributions are associated with each mode, while the c_R distributions change with redshift and mass bin. The relative scaling of each mode also changes with the redshift and mass bin, with more fast-mode SNe at lower redshift and higher mass.

these biases are still mild in any one realization, and these parameters do not have much correlation with cosmological parameters, we decided to accept UNITY1.8 as an overall improvement over current models and proceed to unblinding, although more investigation is needed.

3.4. Checks with the Predictive Posterior Distributions

One way to look for any improvement in model fidelity between UNITY1.7 and 1.8 is to test with the predictive posterior distributions. These are datasets that are simulated from the model posterior distribution. For each MCMC sample, we simulate a dataset from the UNITY model, including simulating which SNe are discovered and selected to be in the final sample according to the modeled efficiency of each survey. As in Rubin et al.

(2025), we approximate the light-curve-fit uncertainties by constructing an interpolation for each SN of m_B , x_1 , c uncertainties based on the true m_B and c (x_1 has a smaller effect on the uncertainties, which we ignore).

We make three figures comparing these predictive-posterior distributions with the actual data. Figure 2 compares the m_B (minus distance modulus $\mu(z)$ for flat Λ CDM), x_1 , and c predictive posterior and data distributions in five redshift bins containing equal numbers of SNe. It compares the single-mode UNITY1.7 with the two-mode UNITY1.8, with UNITY1.8 matching the data generally better. To give a sense of the improvement, the total χ^2 value improves by 29 from UNITY1.7 to 1.8 across all panels (although the exact value will depend on the binning), so UNITY1.8 models the data much better than UNITY1.7. UNITY1.8 still misses some features of the data (notably the very low redshift x_1 distribution), but we have tested that adding yet another Gaussian mode does not affect the cosmology; see Section 3.5. Figure 3 shows Hubble residuals plotted against observed x_1 in two redshift bins for both UNITY1.7 and UNITY1.8. These results show that UNITY1.8 standardizes almost the entire x_1 range well (i.e., $x_1 > -2$), and even $x_1 \sim -2.5$ SNe are standardized much better with UNITY1.8 than 1.7. Figure 4 parallels the plots for c . These results show a good match to the data for both UNITY1.7 and 1.8.

3.5. Cosmology Unblinding Procedure

Before unblinding, the co-authors agreed upon a set list of variants on the nominal UNITY1.8 model. These variations of the nominal model were designed primarily to gauge the sensitivity of cosmological parameters to slight adjustments in how we modeled the x_1 and color distributions, as well as the resultant standardization. The variants of the nominal UNITY1.8 model we considered were decided upon as (nearly) equally well motivated equivalents to the nominal model. These were:

1. The addition of a third superposed Gaussian to the nominal, two-mode description of the x_1/c distributions. This was motivated by the large width of the fast-mode x_1 distribution and the observation that the mean of the fast-mode x_1 distribution shifts to lower values for the oldest populations (Larison et al. 2024). We linked the α values of the two lower- x_1 modes, essentially using the new mode to help model the x_1 distribution of the fast-mode SNe.
2. Splitting β_B by P^{slow} instead of having only one β_B value for both modes. We found consistency between the fast-mode β_B and the value from the

slow mode, and so did not choose to make this split in the nominal model.

3. Splitting β_R by P^{slow} instead of $P_{\text{eff}}^{\text{high}}$. This is similar to the Wojtak et al. (2023) model. For this model, the host-stellar-mass step is not found to be zero. Ultimately, this motivated us to run another variant (after unblinding) which splits β_R on both mode and host stellar mass, discussed below.

Before deciding whether to unblind UNITY1.8, we first verified that each of the variants had minimal impact on the inferred cosmology, namely Ω_m for flat Λ CDM, as well as w_0-w_a when including BAO and CMB data (external cosmological constraints are discussed in Section 5.2). The results are shown as the boxed nominal model and the three markers to the right in all rows of Figure 5. The cosmology inferred by UNITY1.8 and the adopted variants matches the nominal model to better than 0.25σ , despite one of the model variants—the one that splits β_R on P^{slow} rather than $P_{\text{eff}}^{\text{high}}$ —leading to significant shifts in the host-mass-dependent standardization parameters. If the deviation had exceeded $\sim 0.3\sigma$, we would have delayed unblinding and continued to evaluate the merits of different models at the SN standardization level before revisiting the unblinding stage. That was not the case and so we locked in the nominal model and unblinded UNITY1.8.

After unblinding, we decided to run another UNITY1.8 variant: having a separate β_R for fast-mode SNe, but still splitting β_R for slow-mode SNe by host-galaxy mass. This model might be motivated if progenitor age were a meaningful predictor of β_R among high-stellar-mass host galaxies, i.e., if young SNe in high-stellar-mass hosts had β_R values more like young SNe in low-stellar-mass hosts. Interestingly, we find that the slow-mode SNe hosted by high-stellar-mass galaxies have a β_R consistent with the fast-mode SNe (most of which are in high-stellar-mass galaxies). Thus, β_R really does seem to be a stronger function of host-galaxy stellar mass than the slow/fast mode. The results of this model are shown in the right column of Figure 5. In short, the host-mass-step ($\delta(z=0)$) is still consistent with zero (discussed in Section 4.4), and the cosmological constraints actually show slightly more tension with flat Λ CDM than the nominal model.

We discuss the nominal-model unblinded cosmology results for the remainder of this article.

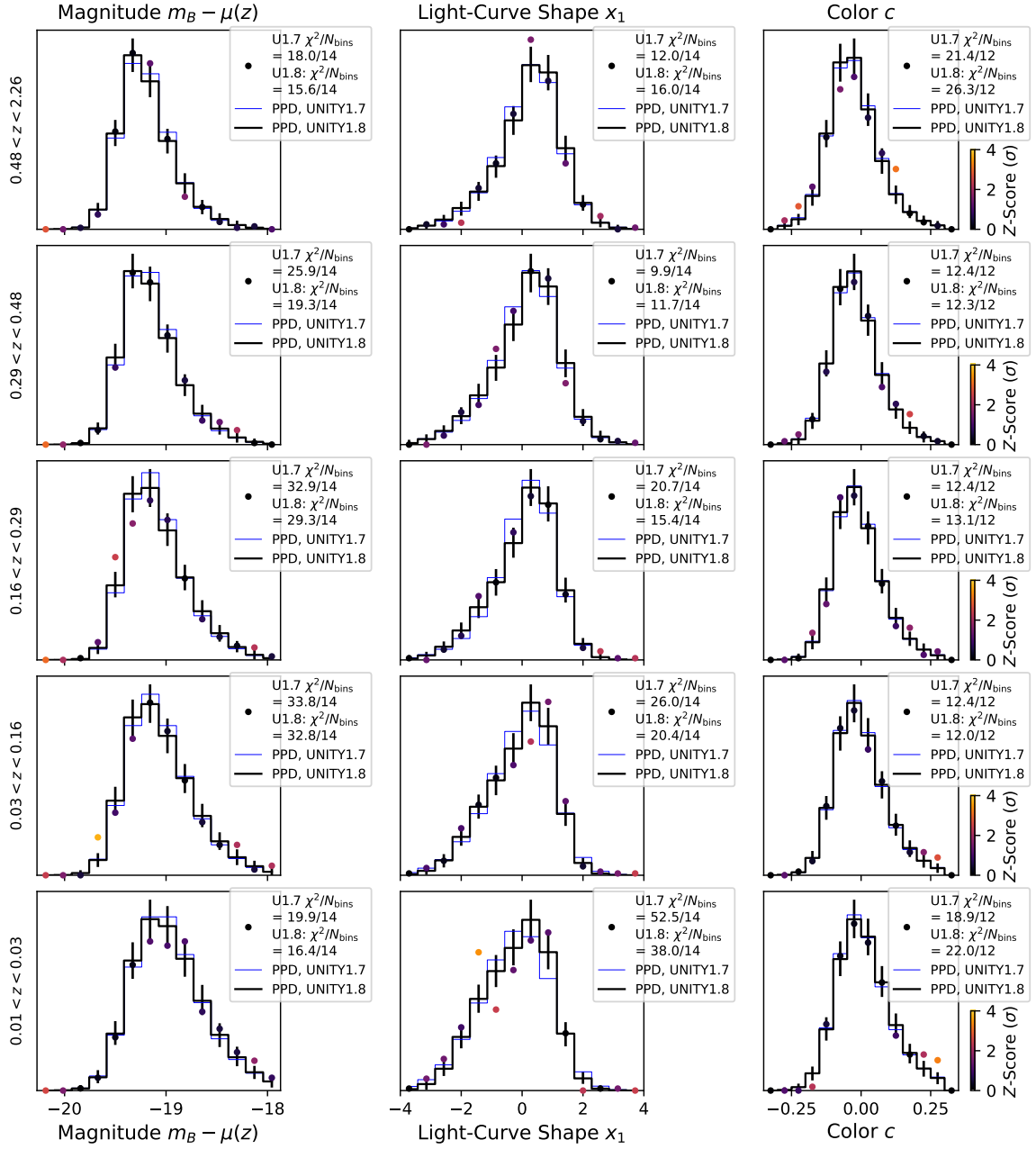


Figure 2. Histograms of the predictive posterior distribution $m_B - \mu(z)$, x_1 , c (columns) in bins of redshift (rows) compared to the actual data. The UNITY1.7 distributions are plotted with thin blue lines; the UNITY1.8 distributions are plotted with thick black lines with error bars. The data are plotted with points, color-coded by the z score of the point and the legends give the total $\chi^2 = \sum z^2$. As seen in Rubin et al. (2025), many of the points making large contributions to the χ^2 are from bins with a small number of events and so will not have much weight in the analysis. UNITY1.8 cuts off at high x_1 faster than UNITY1.7 and correctly models a flatter-top distribution at low redshift, despite having fewer parameters. To give a sense of the improvement, the total χ^2 value improves by 29 from UNITY1.7 to 1.8 across all panels (although the exact value will depend on the binning), so UNITY1.8 models the data much better than UNITY1.7. UNITY1.8 still misses some features of the data (notably the very low redshift x_1 distribution), but we have tested that adding yet another Gaussian mode does not affect the cosmology; see Section 3.5.

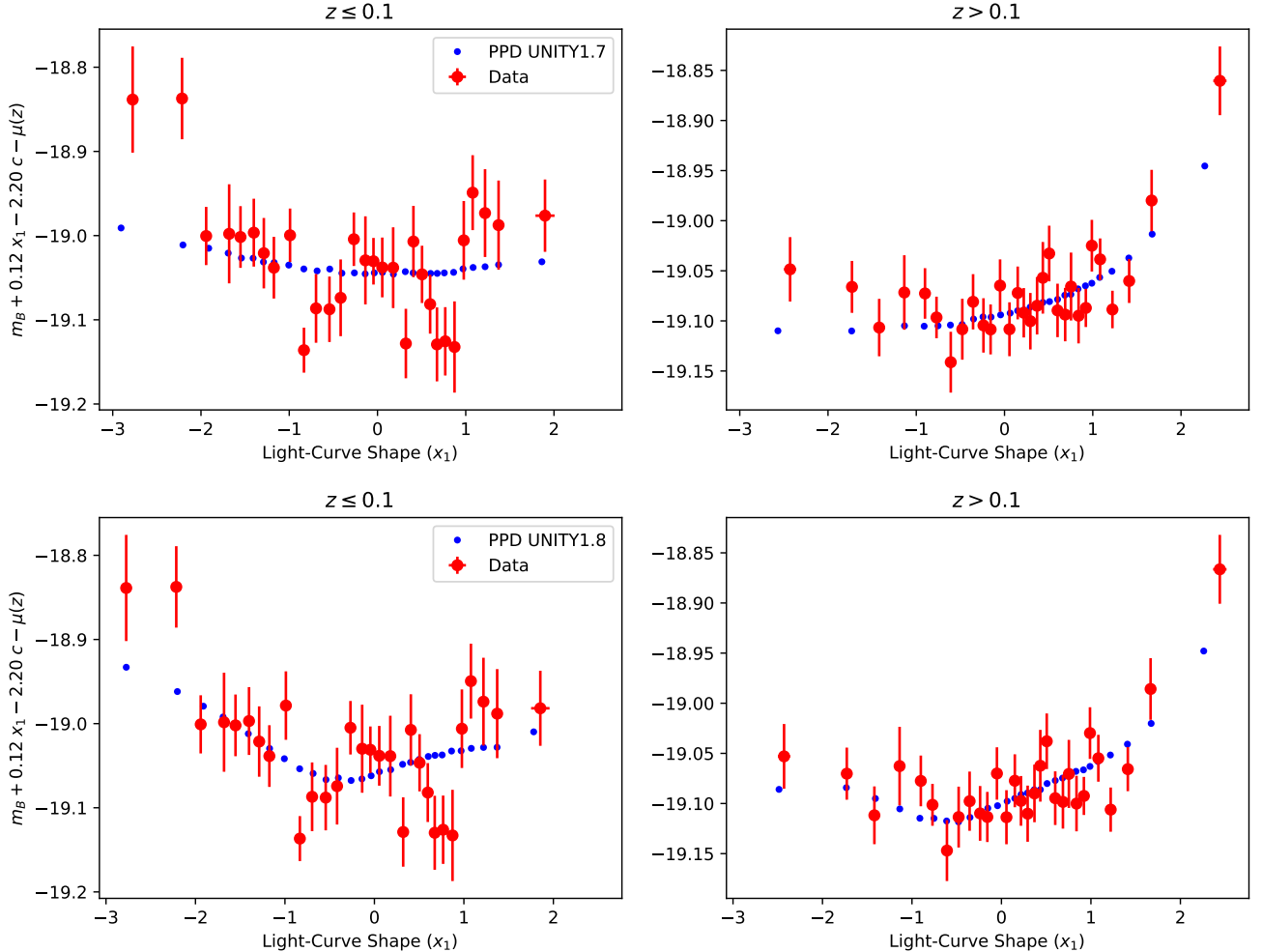


Figure 3. A comparison of Tripp (1998) Hubble residuals between real data (red dots with uncertainties) and the predictive posterior distribution (PPD, blue dots) in 30 x_1 bins with (roughly) equal numbers of SNe. We choose x_1 and c coefficients that give roughly flat relations when plotted against x_1^{obs} and c^{obs} (these coefficients will be smaller than the α 's and β 's due to regression dilution). To give a sense of the impact on cosmology, the **left panels** show $z \leq 0.1$ while the **right panels** show $z > 0.1$. The **top panels** show the single-mode UNITY1.7 results while the **bottom panels** show the two-mode UNITY1.8 results. These results show that UNITY1.8 standardizes almost the entire x_1 range well (i.e., $x_1 > -2$), and even $x_1 \sim -2.5$ SNe are standardized much better with UNITY1.8 than 1.7.

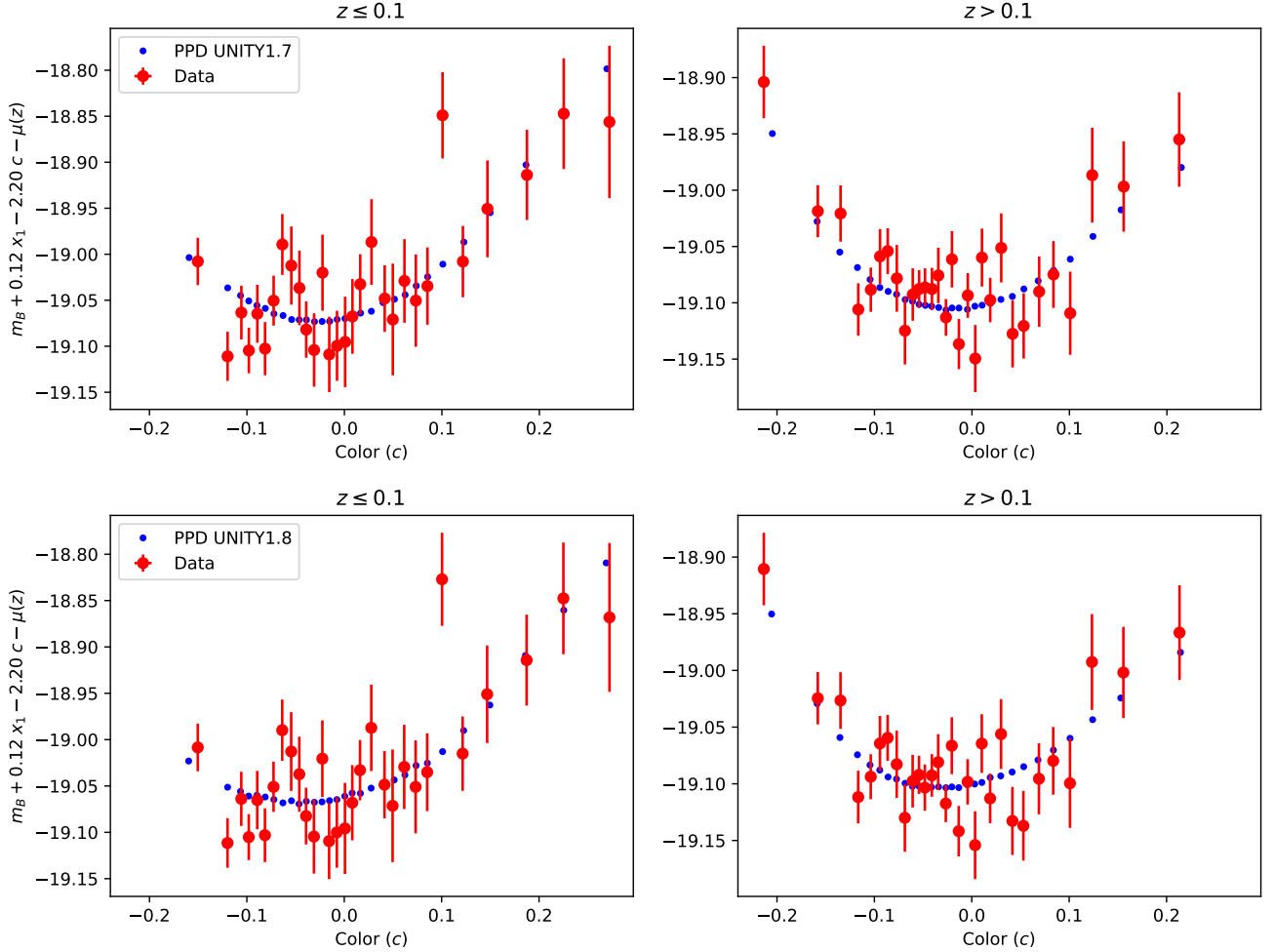


Figure 4. A comparison of Tripp (1998) Hubble residuals between real data (red dots with uncertainties) and the predictive posterior distribution (PPD, blue dots) in 30 color bins with (roughly) equal numbers of SNe. To give a sense of the impact on cosmology, the **left panels** show $z \leq 0.1$ while the **right panels** show $z > 0.1$. The **top panels** show the single-mode UNITY1.7 results while the **bottom panels** show the two-mode UNITY1.8 results. These results show a good match to the data for both UNITY1.7 and 1.8.

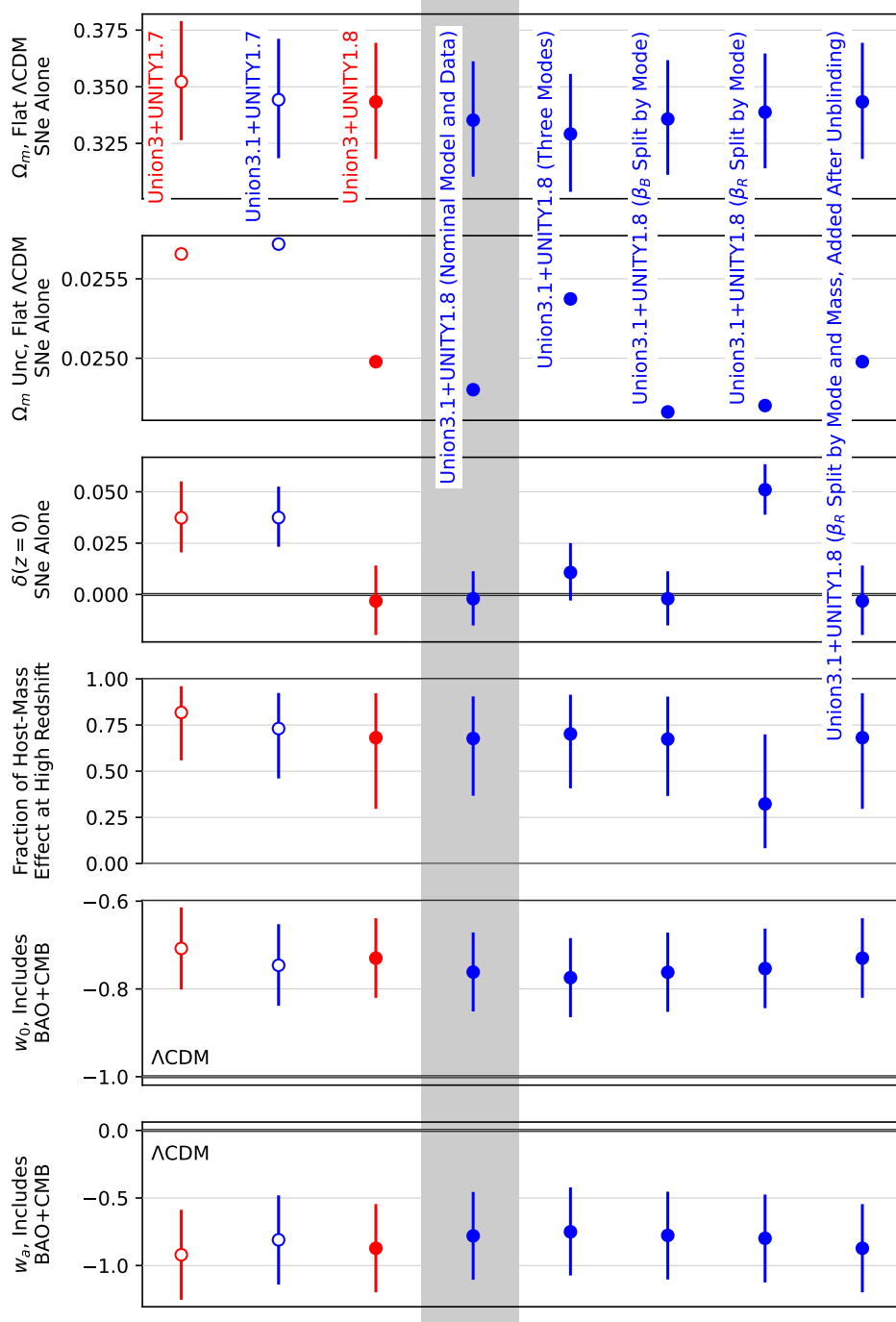


Figure 5. Tracking the inference of standardization and cosmological parameters across the versions of Union and UNITY discussed in this work. The central gray rectangle denotes our suggested nominal UNITY1.8 model. Red (blue) points are based on the Union3 (Union3.1) compilation. Outlined (filled) points correspond to UNITY1.7 (UNITY1.8) runs. Points to the right of the rectangle (except the rightmost one) track the UNITY1.8 variant models that were confirmed to return consistent cosmologies before we unblinded. The leftmost two points show the impact of switching from Union3 to Union3.1 and were taken from Hoyt et al. (2026). It is important to note that all UNITY1.8 variants that enable different β_R values with host-galaxy mass (all filled points except the second rightmost one) obtain a mass step (δ) value consistent with zero. It is also very interesting to note that UNITY1.7 (outlined points) gets cosmological results within uncertainties of UNITY1.8, even though its population assumptions do not match the data as well as UNITY1.8's (only one population mode rather than two). It is also interesting to note that all UNITY1.8 variants return (slightly) smaller Ω_m uncertainties than UNITY1.7 when run with the same input data. (In other words, all the filled points have smaller Ω_m uncertainties than the corresponding outlined points.)

4. SUPERNOVA MODELING RESULTS AND IMPLICATIONS

Here, we summarize the SN-focused results from running UNITY1.8 on Union3.1. Figure 6 shows a corner plot of many of the parameters related to standardization and Table 2 shows 68% credible intervals for a more complete set. Many of UNITY1.8’s supernova results agree with previous results in broad strokes, but with some differences and some significant improvements. Our posteriors show strong evidence for two population modes (Section 4.1). The x_1 standardization varies between the two modes, discussed in Section 4.2. We continue to see evidence of differences in color standardization between red and blue SNe and between SNe in low-mass and high-mass host galaxies, discussed in Section 4.3. Importantly, UNITY1.8 eliminates the host-mass/luminosity correlation, discussed in Section 4.4. The two modes have very different unexplained dispersions, with the slow-mode SNe having less, discussed in Section 4.5. Finally, it is important to note that UNITY1.8 is an empirical model based on the empirical SALT3 (Kenworthy et al. 2021; Taylor et al. 2023) light-curve fit results, and some of our conclusions could easily reflect specific properties of SALT3 and not SNe Ia in general. Validation of our conclusions will require exploration with other light-curve fitters. Ideally, one would bring the light-curve fitting and training inside UNITY so there is no information compression due to light-curve fitting.⁵

4.1. Statistical Evidence for Two Populations

As with the previous studies motivating this paper (discussed in the Introduction and Section 3.1), we find strong evidence of two modes, i.e., f^{slow} is not 0 and also not 1. Both modes are especially noticeable for high host stellar mass ($> 10^{10} M_{\odot}$) and for the larger samples sizes at low- z ($f^{\text{slow}} = 0.294^{+0.039}_{-0.040}$) and mid- z ($f^{\text{slow}} = 0.472 \pm 0.041$).

4.2. x_1 Population and Standardization

We find evidence for two distinct values of α for the two modes: $\alpha^{\text{fast}} = 0.242^{+0.016}_{-0.015}$, $\alpha^{\text{slow}} = 0.169^{+0.013}_{-0.012}$. There is good consistency in the literature for α^{fast} (or α for low- x_1 SNe), but there is more disagreement for α^{slow} . Our value for α^{fast} agrees within uncertainties

with the α value measured in bins below, above and in the range $10^{10} < M_{\odot}^{\text{host}} < 10^{11}$ by Garnavich et al. (2023, Fig 7). Ginolini et al. (2025a) report for a volume-limited ZTF DR2 sample a global $\alpha = 0.161 \pm 0.010$ and for a broken-alpha standardization law with break point $x_1 = -0.48 \pm 0.08$, $\alpha^{\text{slow}} = 0.083 \pm 0.009$ and $\alpha^{\text{fast}} = 0.271 \pm 0.011$. In an analysis of sibling SNe in ZTF DR2, Dhawan et al. (2024) found a larger global $\alpha = 0.228 \pm 0.029$ using ZTF DR2 data than did the full ZTF analysis, which they show is due to sibling occurrences preferring lower- x_1 (faster declining) SNe. They also enforce an x_1 split equal to that found by Ginolini et al. and find $\alpha^{\text{slow}} = 0.133 \pm 0.072$ and $\alpha^{\text{fast}} = 0.274 \pm 0.045$. Newman et al. (2025) report an $\alpha = 0.209 \pm 0.015$ for a narrow selection of SNe with $-2.0 < x_1 < 0.0$ and $-0.2 < c < 0.1$.

4.3. Color Population and Standardization

Union3.1+UNITY1.8 finds distinct values of β between blue SNe, red SNe in low-stellar-mass galaxies, and red SNe in high-stellar-mass galaxies. The bluest SNe have the shallowest magnitude-color relation ($\beta_B = 2.12^{+0.17}_{-0.16}$). For redder SNe, we find a significant β_R split between low- and high-stellar-mass host galaxies: β_R in low-mass hosts is $4.56^{+0.19}_{-0.17}$, while for high-mass at low redshift, it is $3.34^{+0.13}_{-0.12}$ (mean $\beta_R = 3.95^{+0.13}_{-0.12}$, $\Delta\beta_R = -1.22 \pm 0.19$). Union3+UNITY1.5 found consistent values although with much larger uncertainties due mostly to the bug in the outlier color width parameter limit discussed in their Appendix B: $\beta_B = 2.6 \pm 0.4$, $\beta_R = 3.62^{+0.21}_{-0.18}$, and $\Delta\beta_R = -1.1^{+0.3}_{-0.4}$. For comparison to extinction-law R_V values, we remind the reader that $R_V \approx R_B - 1$ so one expects $\beta_R \approx 4$ if it is driven by Milky-Way-like dust extinction ($R_V \approx 3.1$, Savage & Mathis 1979).

The values of β_R are similar to those from the Wojtak et al. (2023) and Wojtak & Hjorth (2025) models, with Wojtak & Hjorth (2025) finding their \widehat{R}_B values of $4.074^{+0.510}_{-0.494}$ and 3.030 ± 0.117 for their slow and fast decliner subpopulations, compared to our $4.56^{+0.19}_{-0.17}$ and $3.34^{+0.13}_{-0.12}$ for β_R in low- and high-mass host galaxies. The agreement tightens when we adjust the UNITY model to split β_R on x_1 mode, similar to Wojtak & Hjorth (2025), rather than on mass as in our nominal model. This results in values of β_R equal to $4.13^{+0.14}_{-0.13}$ and $3.27^{+0.17}_{-0.16}$ for the slow-mode and fast-mode populations, respectively.

In Figure 7, we plot the latent c_B^{true} and c_R^{true} values inferred by UNITY for each SN as a function of the SALT3 color parameter c^{obs} from the Union3.1 light-curve fits. The y -coordinate of the top distribution of points is c_R , while that of the bottom distribution is c_B . Each marker

⁵ Even more ideally, one would compare observations directly against physical models of SNe Ia (e.g., Hoeflich & Khokhlov 1996). However, this will require quantifying and controlling the uncertainties of those models.

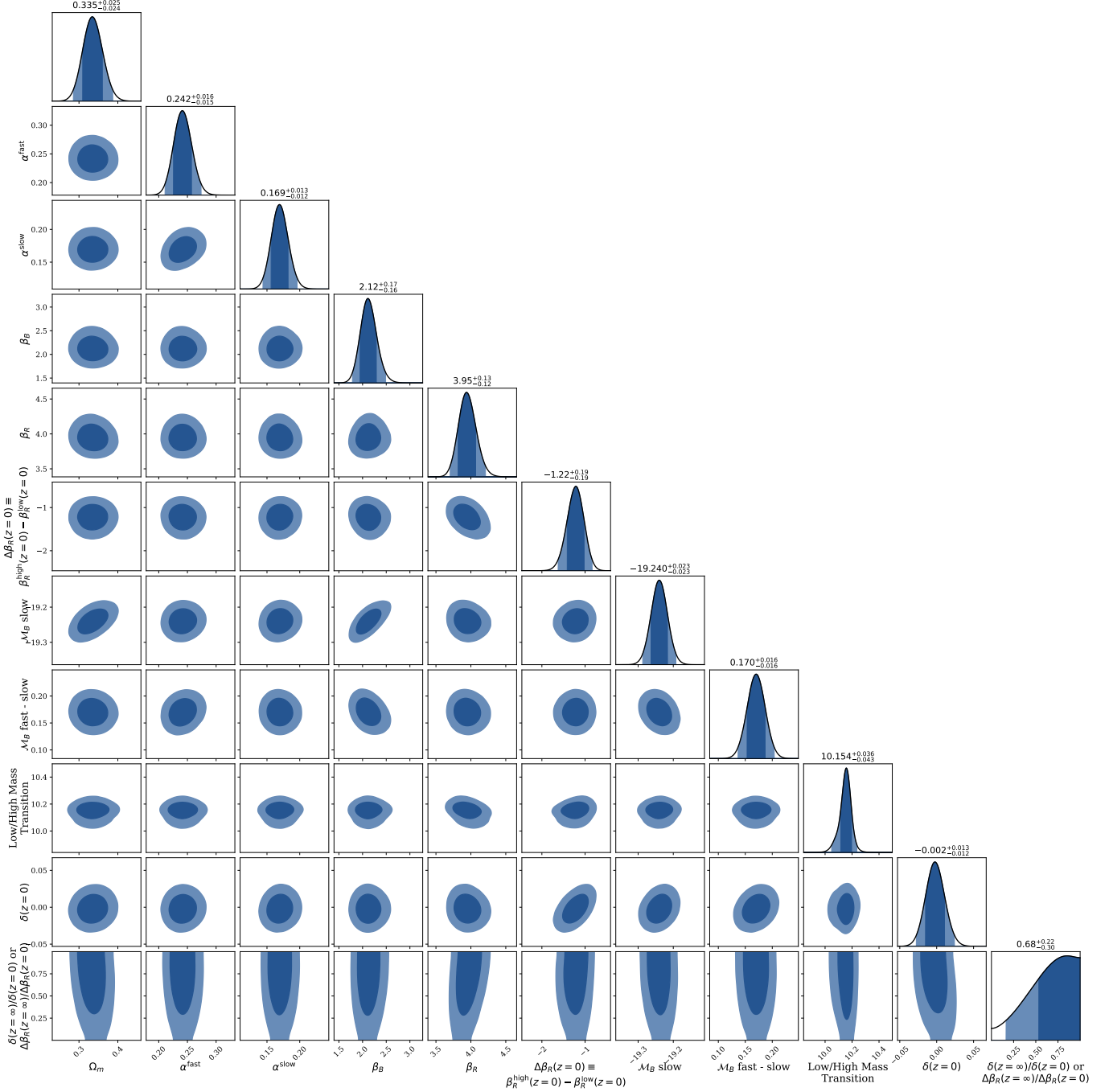


Figure 6. Corner plot of standardization parameters from Equation 9. We observe significantly different x_1 -standardization relations (α) between the two modes, three distinctly different color-standardization relations (β), and a host-mass/luminosity step consistent with zero ($\delta(z = 0) = 0$, thus zero for all redshifts by Equation 2). See Table 2 for a more complete list of parameters.

Table 2. 68.3% credible intervals for UNITY1.8 parameters.

Parameter	Posterior
\mathcal{M}_B slow-mode	$\mathcal{M}_B^{\text{slow}} = -19.240 \pm 0.023$ (mag)
\mathcal{M}_B fast-mode – \mathcal{M}_B slow-mode	$\mathcal{M}_B^{\text{fast-slow}} = 0.170 \pm 0.016$ (mag)
fast-mode α	$\alpha^{\text{fast}} = 0.242_{-0.015}^{+0.016}$ (mag per x_1)
slow-mode α	$\alpha^{\text{slow}} = 0.169_{-0.012}^{+0.013}$ (mag per x_1)
β for blue, Gaussian-distributed color	$\beta_B = 2.12_{-0.16}^{+0.17}$ (mag per mag)
β for red, exponentially distributed color in high-mass hosts	$\beta_R^{\text{high}} = 3.34_{-0.12}^{+0.13}$ (mag per mag)
in low-mass hosts	$\beta_R^{\text{low}} = 4.56_{-0.17}^{+0.19}$ (mag per mag)
β_R difference with host mass	$\Delta\beta_R \equiv \beta_R^{\text{high}} - \beta_R^{\text{low}} = -1.22 \pm 0.19$ (mag per mag)
\log_{10} host-galaxy mass at step	$= 10.154_{-0.043}^{+0.036}$ ($\log_{10} M_\odot$)
host-mass-luminosity step at low redshift	$\delta(z=0) = -0.002_{-0.012}^{+0.013}$ (mag)
fraction of host-mass correlations remaining at high redshift	$\delta(z=\infty)/\delta(z=0) = 0.68_{-0.30}^{+0.22}$ (mag per mag)
	$= \Delta\beta_R(z=\infty)/\Delta\beta_R(z=0)$
outlier fraction	$f^{\text{outl}} = 0.0127_{-0.0028}^{+0.0033}$
slow-mode unexplained dispersion, mean of SN samples	$< \sigma^{\text{unexpl., slow}} > = 0.1188_{-0.0097}^{+0.0098}$
extra fast-mode unexplained dispersion, added in quadrature	$\sigma^{\text{unexpl., fast}} = 0.084_{-0.013}^{+0.012}$
fraction unexplained variance in m_B	$f^{m_B} = 0.38 \pm 0.13$
fraction unexplained variance in x_1	$f^{x_1} = 0.126_{-0.035}^{+0.041}$
fraction unexplained variance in c	$f^c = 0.49 \pm 0.12$
Gaussian x_1 peak, fast-mode	$x_1^{\text{*, fast}} = -0.916 \pm 0.068$ (x_1)
slow-mode	$x_1^{\text{*, slow}} = 0.547 \pm 0.032$ (x_1)
Gaussian x_1 width, fast-mode	$R_{x_1}^{\text{fast}} = 0.827_{-0.038}^{+0.039}$ (x_1)
slow-mode	$R_{x_1}^{\text{slow}} = 0.489 \pm 0.026$ (x_1)
Gaussian c_B peak, fast-mode	$c^{\text{*, fast}} = -0.0465 \pm 0.0081$ (mag)
slow-mode	$c^{\text{*, slow}} = -0.0818 \pm 0.0067$ (mag)
Gaussian c_B width, fast-mode	$R_c^{\text{fast}} = 0.0571_{-0.0054}^{+0.0052}$ (mag)
slow-mode	$R_c^{\text{slow}} = 0.0391 \pm 0.0032$ (mag)
exponential c_R scale, low- z , high-mass	$\tau_{c_R} = 0.0868_{-0.0063}^{+0.0070}$ (mag)
mid- z , high-mass	$\tau_{c_R} = 0.0763_{-0.0054}^{+0.0058}$ (mag)
high- z , high-mass	$\tau_{c_R} = 0.072_{-0.016}^{+0.020}$ (mag)
low- z , low-mass	$\tau_{c_R} = 0.0802_{-0.0084}^{+0.0094}$ (mag)
mid- z , low-mass	$\tau_{c_R} = 0.0610_{-0.0047}^{+0.0051}$ (mag)
high- z , low-mass	$\tau_{c_R} = 0.062_{-0.020}^{+0.026}$ (mag)
fraction in slow mode, low- z , high-mass	$f^{\text{slow}} = 0.294_{-0.040}^{+0.039}$
mid- z , high-mass	$f^{\text{slow}} = 0.472 \pm 0.041$
high- z , high-mass	$f^{\text{slow}} = 0.54_{-0.17}^{+0.16}$
low- z , low-mass	$f^{\text{slow}} = 0.795_{-0.053}^{+0.048}$
mid- z , low-mass	$f^{\text{slow}} = 0.881_{-0.030}^{+0.027}$
high- z , low-mass	$f^{\text{slow}} = 0.85_{-0.17}^{+0.10}$

represents a single SN and each SN appears twice on this plot (one in each color distribution). In this plane, we see that fast-declining SNe Ia are associated with redder (bluer) values of c_B (c_R) than slow-declining ones. This finding is consistent with faster-declining SNe occurring more frequently in passive galaxy environments and that they appear to have redder intrinsic colors (Garnavich et al. 2004; Ginolini et al. 2025b).

4.4. Host Correlations

One of our most important results is that we find $\delta(z=0) = -0.002^{+0.013}_{-0.012}$ mag for Union3.1+UNITY1.8, i.e., there is no longer an explicit luminosity step as a function of host-galaxy stellar mass for unreddened SNe. A host-stellar-mass step consistent with zero is a unique result⁶ that may indicate that much of what has been considered the host-mass relation is due to previous models conflating two distinct subtypes of SNe Ia which have different relative frequencies as a function of host stellar mass and redshift (likely due to different delay-time distributions, e.g., Wiseman et al. 2021). Noting that this is true for “unreddened SNe” is important as β_R still depends on host mass in our nominal model, so host mass still has some effect for reddened SNe. Figure 5 shows that making β_R a function of the two modes (rather than host stellar mass) gives an apparent luminosity step, so the host galaxy must affect either the color standardization or the magnitude standardization; splitting the SNe by mode is not enough.

We measure the host-galaxy stellar-mass-step location to be $10.154^{+0.036}_{-0.043}$ ($\log_{10}M_\odot$), a small but statistically significant difference from $10^{10}M_\odot$ (this step location controls the β_R stellar-mass-step location as well as the luminosity step location, so it is well constrained). Fortunately for past results, there is very little covariance between this value and Ω_m .

We do not see any evidence of evolution in the host-stellar-mass luminosity and β_R relations with redshift, although our constraints are weak and not very Gaussian; at high redshift, we find $0.68^{+0.22}_{-0.30}$ compared to the low-redshift value of 1 but this is also fairly consistent

⁶ Brout & Scolnic (2021) find no evidence for a stellar-mass step after applying a model with host-stellar-mass-dependent R_V , however the Dark Energy Survey analysis still does find such a step (Vincenzi et al. 2024) using the BS21 model updated by Popovic et al. (2023). However, these are not simultaneous fits and so it is difficult to evaluate the difference between finding a set of parameters that force the stellar-mass step to zero and finding zero as the best fit. In Union3+UNITY1.5, which treats all parameters simultaneously, the inclusion of a split β_R reduces the host-stellar-mass step to 0.031 ± 0.019 mag, but did not eliminate it. Hoyt et al. (2026) finds 0.037 ± 0.014 for Union3.1+UNITY1.7, reproduced in Figure 5 for the same input data we use for UNITY1.8.

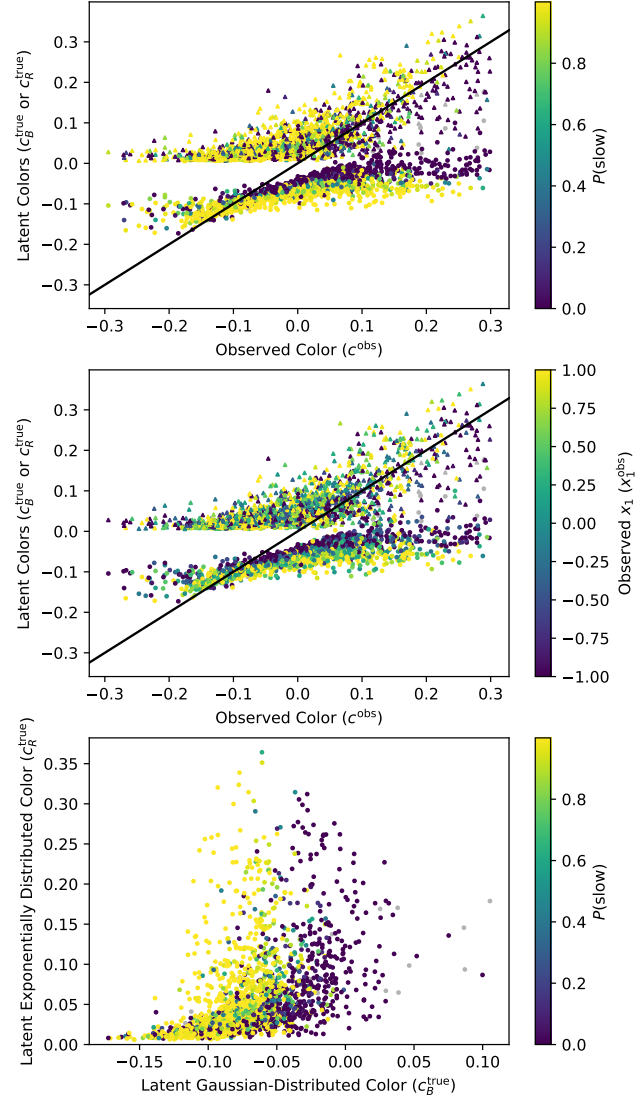


Figure 7. **Top panel:** scatter plot of latent colors (c_B and c_R) as a function of observed color, color coded by P^{slow} . The **middle panel** shows the same plot but color coded by the observed light-curve-shape parameter (x_1). We see that fast-mode/lower x_1 SNe have on average redder Gaussian-distributed c_B colors for all values of observed color (c^{obs}). For red values of the observed color, fast-mode SNe also tend to have c_R colors more similar to c_B than do slow-mode SNe. The **bottom panel** shows c_R^{true} plotted as a function of c_B^{true} , color coded by P^{slow} and clearly shows the difference in c^* for the two modes.

with 0 (which would imply the host-galaxy correlations go away at high redshift).

4.5. Unexplained Dispersions

Figure 8 shows the 68.3% credible intervals for the unexplained-dispersion parameters for each SN sample for both UNITY1.7 and UNITY1.8. UNITY1.7 has one unexplained-dispersion parameter for each sam-

ple while UNITY1.8 has one parameter per sample for the slow mode, then another parameter $\sigma^{\text{unexpl., fast}} = 0.084^{+0.012}_{-0.013}$ for all the samples that is added in quadrature for the fast-mode SNe. (Our motivation for keeping this value the same for all samples is that we expect most of the variation sample-to-sample to be due to inaccuracies in assigned photometry uncertainties rather than differences in SNe with sample selection.) This figure shows generally small ($\lesssim 0.05$ magnitudes) unexplained dispersion for the slow-mode SNe measured from rolling surveys and thus have many SN-free “reference” images (these surveys also typically use scene-modeling photometry for more accurate uncertainties, Holtzman et al. 2008; Astier et al. 2013). We denote rolling surveys with an asterisk. We note that these are inferred values after modeling out the measurement uncertainties and SALT3 model uncertainties. We thus cannot directly tell if the results of our unexplained-dispersion model are intrinsic properties of SNe Ia or just properties of SALT3. UNITY does not make Hubble-residual predictions, so we do not quote a Hubble-diagram dispersion. (We have also not considered whether it would be possible in a dataset with realistic uncertainties to select a pure sample of unreddened slow-mode SNe that may be seen to have lower dispersion.)

Figure 9 shows the allocation of unexplained variance between m_B , x_1 , and c . Compared to Union3+UNITY1.5, we find a shift of unexplained dispersion from c to m_B , resulting in an almost equal fraction of variance between the two (fraction for m_B is 0.38 ± 0.13 , fraction for c is 0.49 ± 0.12 , with the remaining $0.126^{+0.041}_{-0.035}$ in x_1). Using Kessler et al. (2013) Figure 11 to roughly compare against two frequently used scatter models, we find this result is in between the Guy et al. (2010) and Chotard et al. (2011) models, although more similar to Guy et al. (2010). One of the Chotard et al. (2011) spectral components is aligned with x_1 , which UNITY1.8 does a better job modeling, so it is not clear whether this is an unexpected result.

5. COSMOLOGY RESULTS

5.1. SN Cosmology Results

As in Union3+UNITY1.5 (Rubin et al. 2025), we compute an approximate distance-modulus covariance matrix with UNITY so that our SN results are easily transferable to other analyses without rerunning UNITY. We put a quadratic spline through a series of spline nodes in redshift (shown in Figure 10) and model the difference in distance modulus between the data and a flat Λ CDM model with $\Omega_m = 0.3$. The values of the spline nodes and their covariance matrix is an excellent approximation to the full UNITY posterior, which can be seen by

comparing the frequentist fits in this Section with the corresponding posteriors in Figure 5 (and as discussed in Rubin et al. 2025).

Figure 10 plots the distance-modulus residuals against three cosmological models: flat Λ CDM with $\Omega_m = 0.3$ (the BAO+CMB best fit, also similar to SN+BAO+CMB), flat Λ CDM with $\Omega_m = 0.334$ (the SN-only best-fit), and a w_0 - w_a model which is the best fit including BAO and CMB constraints. The weak preference of the SN data for a higher flat- Λ CDM Ω_m value is mitigated when fitting a w_0 - w_a model (see also Ó Colgáin & Sheikh-Jabbari 2025), discussed more in Section 5.2.

We compute frequentist contours ($\Delta\chi^2$ compared to the best fit of 2.296, 6.180, and 11.829 for 68.3%, 95.4%, and 99.7% confidence) by fixing the two parameters shown in the plane and fitting for the others. We use an adaptive-refinement contour code that chooses points to evaluate.⁷ Figure 11 compares such contours for Union3+UNITY1.5, Union3.1+UNITY1.7, and Union3.1+UNITY1.8 for flat Λ CDM, and flat Ω_m - w . In general, the three contours show compatible constraints. The contours are completely enclosed for Λ CDM, so we also compute the Figure of Merit (the inverse area of the 2σ contour); our results show Union3.1+UNITY1.8 has a 6% higher FoM than Union3.1/UNITY1.7 (Hoyt et al. 2026) and 15% higher FoM than Union3/UNITY1.5 (Rubin et al. 2025).

5.2. Cosmology Results with External Constraints

Following Rubin et al. (2025), we include BAO, CMB, and/or H_0 constraints and consider flat Λ CDM, Λ CDM with curvature, flat w CDM, flat w_0 - w_a , and w_0 - w_a with curvature. Table 3 presents our best-fit values, 1σ uncertainties, and χ^2 values. Figure 12 shows our constraints in the Ω_m - Ω_Λ plane. Figure 13 shows our constraints in the Ω_m - w plane. As a sanity check of the SN results, Figure 14 shows the combined constraints and the SN-only constraints for flat-universe w_0 - w_a . Figure 15 shows our results in the w_0 - w_a plane (with and without allowing spatial curvature). Figure 16 investigates which individual data combinations drive our w_0 - w_a constraints..

⁷ https://github.com/rubind/adaptive_contour

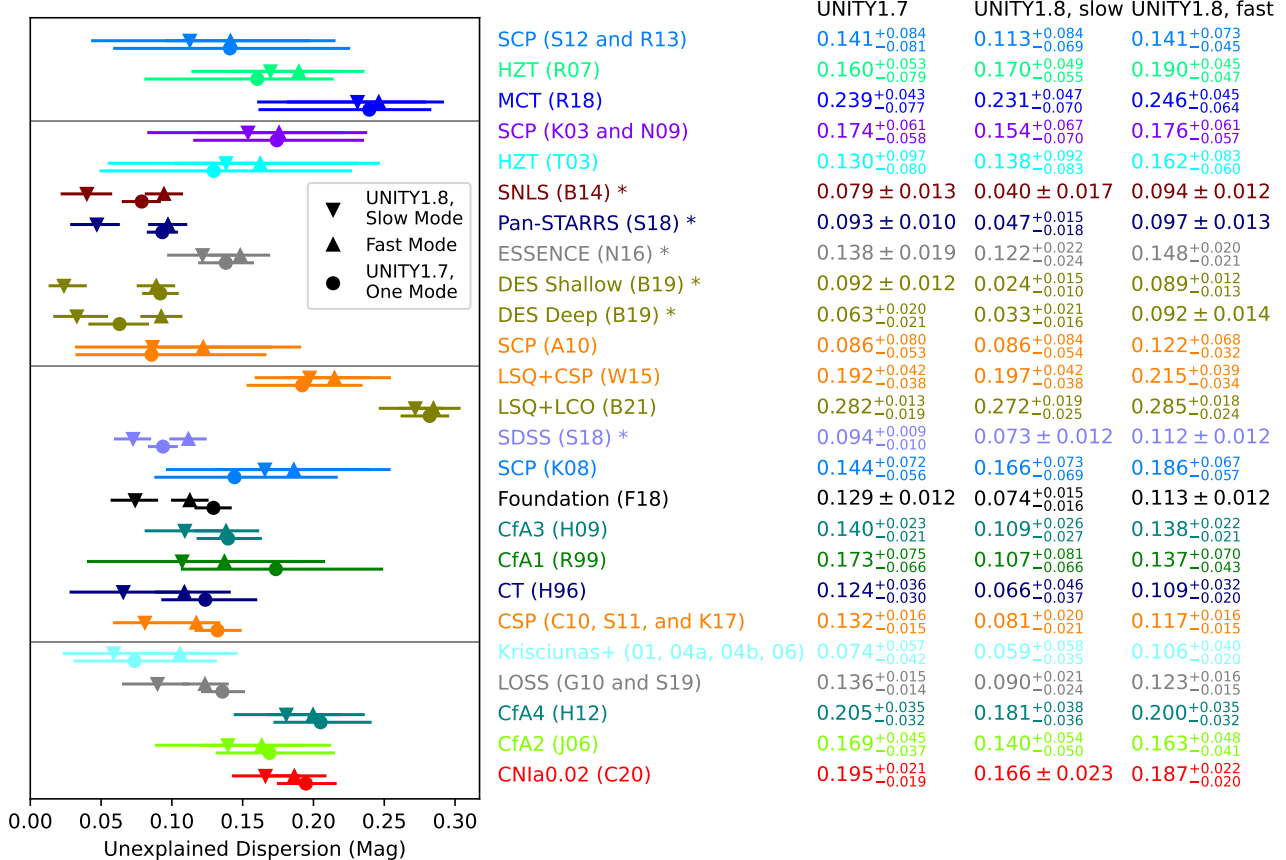


Figure 8. Unexplained dispersion by SN sample for both UNITY1.7 (one population mode) and our recommended UNITY1.8 (with two modes). We find the fast (low- x_1) mode has additional unexplained dispersion, although whether this is due to features of the SALT3 model or whether it is a real property of SNe Ia is not clear. This figure shows generally small ($\lesssim 0.05$ magnitudes) unexplained dispersion for the slow-mode SNe measured from rolling surveys and thus have many SN-free “reference” images (these surveys also typically use scene-modeling photometry for more accurate uncertainties, Holtzman et al. 2008; Astier et al. 2013). We denote rolling surveys with an asterisk.

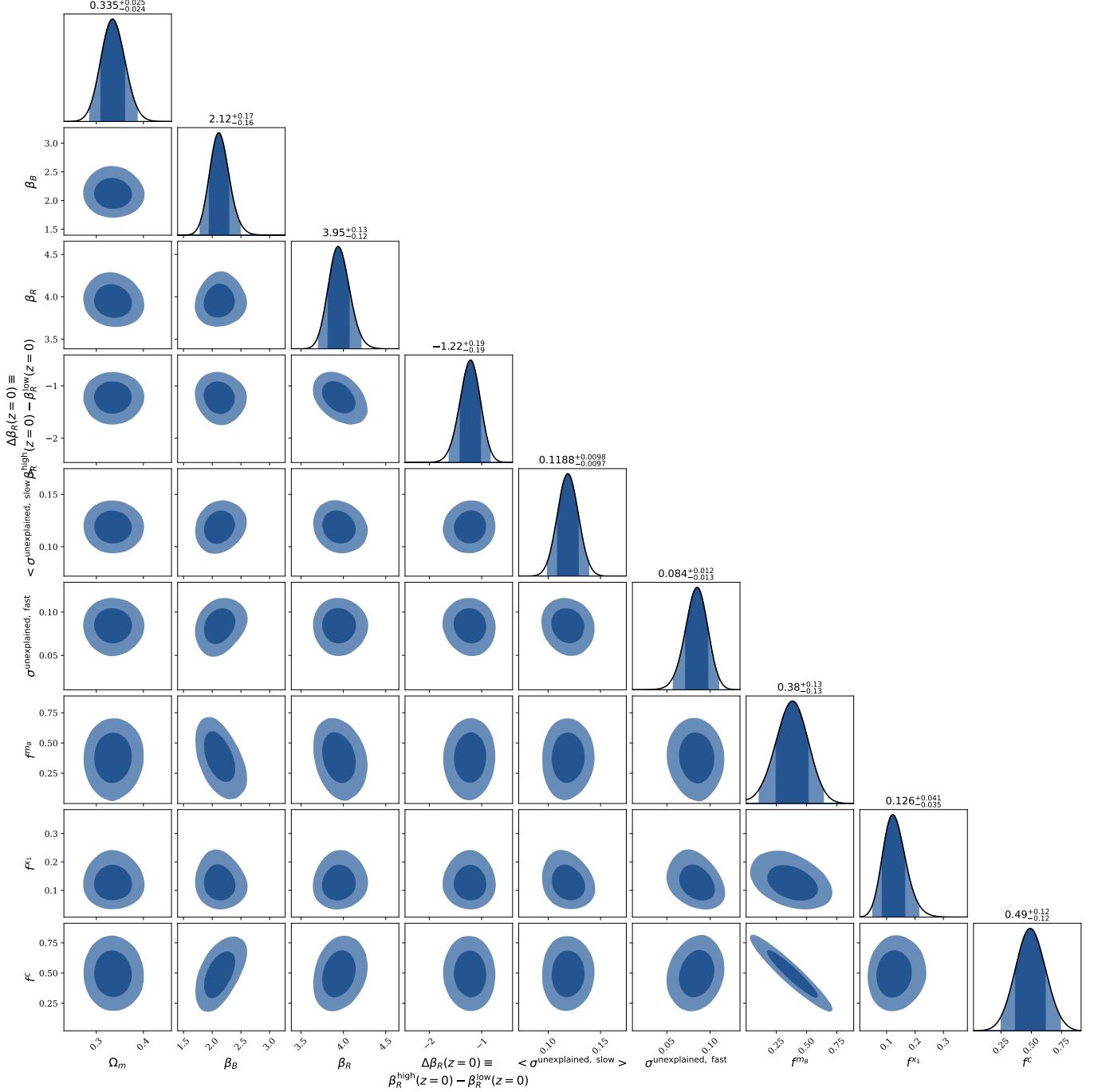


Figure 9. Corner plot of standardization parameters and unexplained dispersion. There is a large degeneracy between the fraction of the unexplained dispersion in magnitude (f^{m_B}) and the fraction in color (f^c), with the fraction in x_1 constrained to be much smaller. As one would expect, putting more unexplained dispersion into color (larger f^c) increases β (especially β_B , which is measured with a smaller color baseline than β_R) because there is more inferred regression dilution.

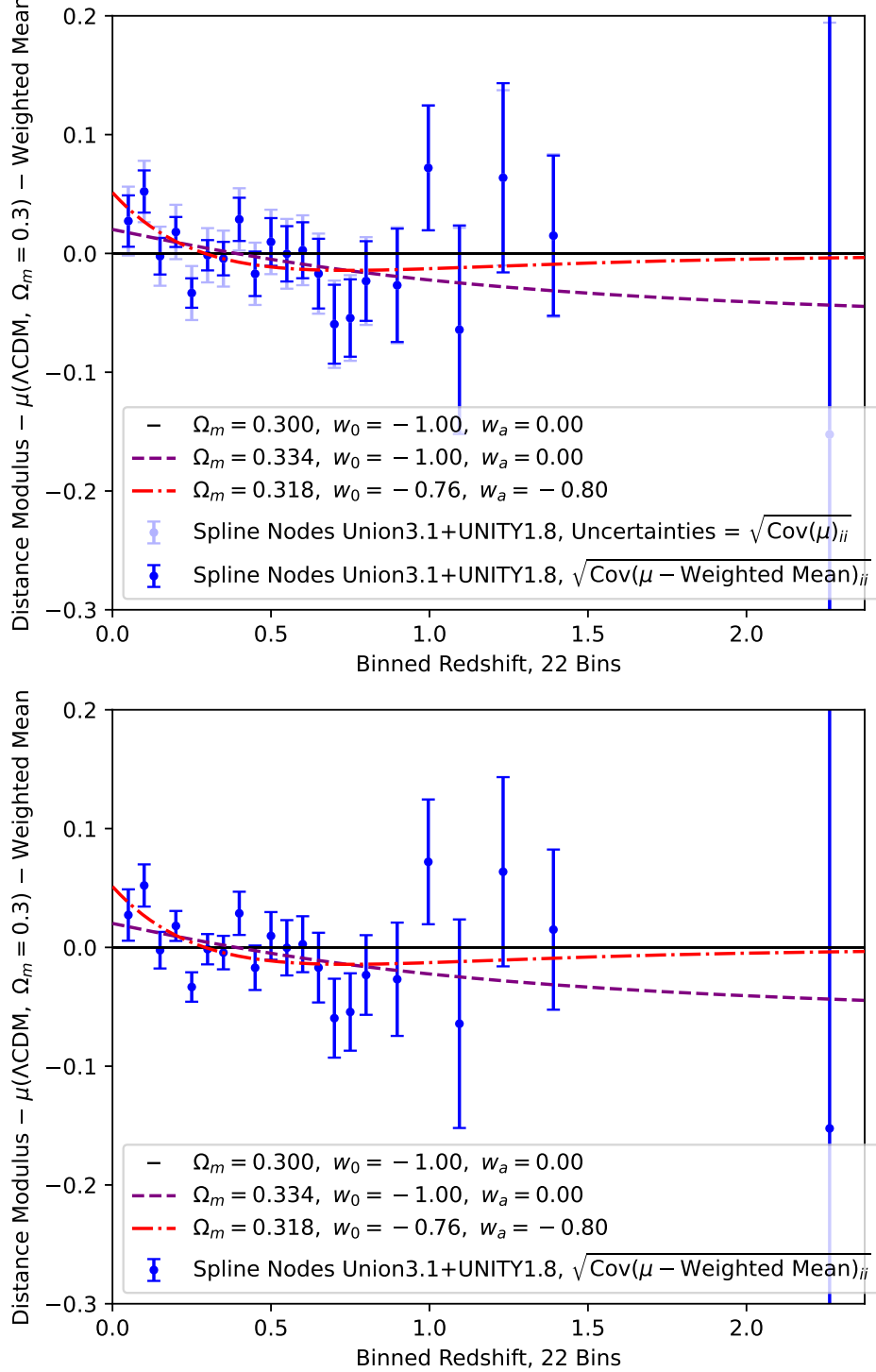


Figure 10. Plots of the UNITY distance-modulus residuals against three cosmological models: flat ΛCDM with $\Omega_m = 0.3$ (black line), flat ΛCDM with $\Omega_m = 0.334$ (the SN-only best-fit, purple dashed line), and a w_0 - w_a model which is the best fit including BAO and CMB constraints (red dot-dashed line). The weak preference of the SN data for a higher flat- ΛCDM Ω_m value is mitigated when fitting a w_0 - w_a model (see also Ó Colgáin & Sheikh-Jabbari 2025), discussed more in Section 5.2.

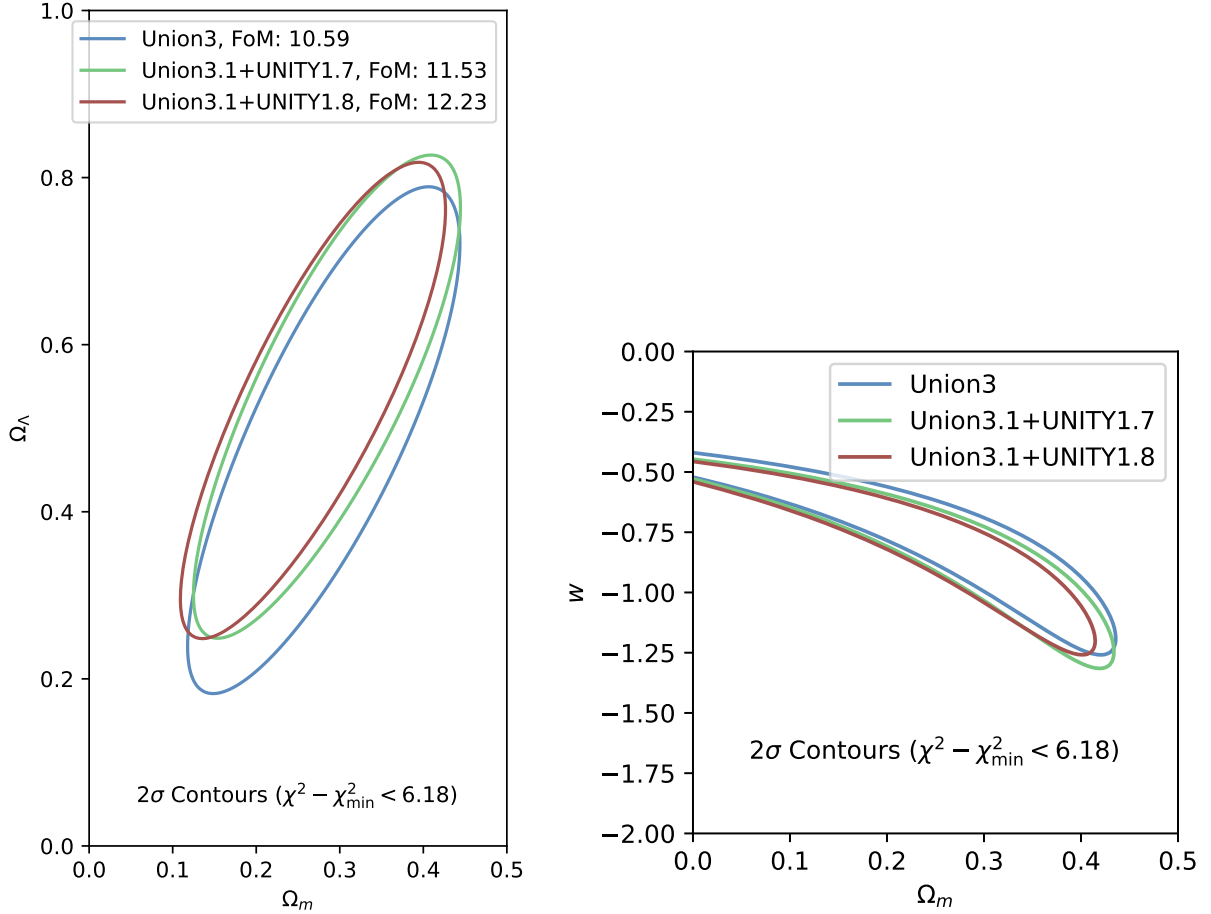


Figure 11. Comparison of SN-only cosmological constraints for Union3+UNITY1.5, Union3.1+UNITY1.7, and Union3.1+UNITY1.8. The **left panel** shows Λ CDM while the **right panel** shows flat Ω_m - w . In all cases, the 2D 2σ contour is plotted (the contour enclosing $\Delta\chi^2 < 6.18$). In general, the three contours show compatible constraints. The contours are completely enclosed for Λ CDM, so we also compute the Figure of Merit (the inverse area of the 2σ contour); our results show Union3.1+UNITY1.8 has a 6% higher FoM than Union3.1/UNITY1.7 (Hoyt et al. 2026) and 15% higher FoM than Union3/UNITY1.5 (Rubin et al. 2025).

Probes	χ^2 (DoF)	h	Ω_m	Ω_k	w or w_0	w_a	DETF	FoM
Flat Λ CDM								
SNe	28.8 (20)	...	$0.334^{+0.025}_{-0.024}$
SNe+CMB	29.3 (21)	$0.673^{+0.006}_{-0.006}$	$0.317^{+0.008}_{-0.008}$
BAO+CMB	14.7 (14)	$0.685^{+0.003}_{-0.003}$	$0.300^{+0.004}_{-0.004}$
SNe+BAO+ ω_b	41.2 (33)	$0.685^{+0.006}_{-0.006}$	$0.301^{+0.008}_{-0.008}$
SNe+BAO+CMB	45.4 (35)	$0.685^{+0.003}_{-0.003}$	$0.301^{+0.004}_{-0.004}$
SNe+BAO+CMB+ H_0^{TRGB}	46.6 (36)	$0.685^{+0.003}_{-0.003}$	$0.300^{+0.004}_{-0.004}$
SNe+BAO+CMB+ $H_0^{\text{Ceph.}}$	72.5 (36)	$0.689^{+0.003}_{-0.003}$	$0.295^{+0.003}_{-0.003}$
Open Λ CDM								
SNe	27.7 (19)	...	$0.274^{+0.063}_{-0.065}$	$0.172^{+0.175}_{-0.166}$
SNe+CMB	28.8 (20)	$0.654^{+0.027}_{-0.025}$	$0.334^{+0.027}_{-0.026}$	$-0.004^{+0.006}_{-0.007}$
BAO+CMB	10.8 (13)	$0.687^{+0.003}_{-0.003}$	$0.302^{+0.004}_{-0.004}$	$0.002^{+0.001}_{-0.001}$
SNe+BAO+ ω_b	40.1 (32)	$0.669^{+0.016}_{-0.016}$	$0.293^{+0.011}_{-0.011}$	$0.039^{+0.038}_{-0.038}$
SNe+BAO+CMB	41.1 (34)	$0.687^{+0.003}_{-0.003}$	$0.303^{+0.004}_{-0.004}$	$0.003^{+0.001}_{-0.001}$
SNe+BAO+CMB+ H_0^{TRGB}	42.0 (35)	$0.688^{+0.003}_{-0.003}$	$0.302^{+0.004}_{-0.004}$	$0.003^{+0.001}_{-0.001}$
SNe+BAO+CMB+ $H_0^{\text{Ceph.}}$	64.9 (35)	$0.692^{+0.003}_{-0.003}$	$0.298^{+0.004}_{-0.004}$	$0.003^{+0.001}_{-0.001}$
Flat w CDM								
SNe	27.2 (19)	...	$0.240^{+0.082}_{-0.109}$...	$-0.776^{+0.158}_{-0.177}$
SNe+CMB	28.3 (20)	$0.663^{+0.012}_{-0.012}$	$0.325^{+0.012}_{-0.012}$...	$-0.960^{+0.041}_{-0.041}$
BAO+CMB	14.3 (13)	$0.690^{+0.009}_{-0.009}$	$0.296^{+0.007}_{-0.007}$...	$-1.022^{+0.037}_{-0.039}$
SNe+BAO+ ω_b	37.0 (32)	$0.656^{+0.015}_{-0.016}$	$0.297^{+0.009}_{-0.009}$...	$-0.898^{+0.049}_{-0.049}$
SNe+BAO+CMB	45.1 (34)	$0.681^{+0.007}_{-0.007}$	$0.303^{+0.006}_{-0.006}$...	$-0.983^{+0.028}_{-0.028}$
SNe+BAO+CMB+ H_0^{TRGB}	46.5 (35)	$0.684^{+0.006}_{-0.006}$	$0.301^{+0.005}_{-0.005}$...	$-0.994^{+0.026}_{-0.027}$
SNe+BAO+CMB+ $H_0^{\text{Ceph.}}$	66.2 (35)	$0.701^{+0.006}_{-0.006}$	$0.287^{+0.004}_{-0.004}$...	$-1.059^{+0.024}_{-0.024}$
Flat w_0 - w_a								
SNe	24.4 (18)	...	$0.443^{+0.061}_{-0.088}$...	$-0.489^{+0.419}_{-0.304}$	$-5.45^{+3.55}_{-4.75}$
SNe+CMB	26.1 (19)	$0.677^{+0.013}_{-0.014}$	$0.312^{+0.014}_{-0.012}$...	$-0.728^{+0.154}_{-0.159}$	$-1.11^{+0.75}_{-0.76}$	1.61	
BAO+CMB	7.9 (12)	$0.646^{+0.019}_{-0.019}$	$0.341^{+0.022}_{-0.021}$...	$-0.532^{+0.230}_{-0.210}$	$-1.40^{+0.61}_{-0.69}$	1.81	
SNe+BAO+ ω_b	34.8 (31)	$0.671^{+0.014}_{-0.016}$	$0.322^{+0.015}_{-0.017}$...	$-0.774^{+0.104}_{-0.099}$	$-0.79^{+0.52}_{-0.53}$	1.98	
SNe+BAO+CMB	35.9 (33)	$0.668^{+0.008}_{-0.008}$	$0.318^{+0.008}_{-0.008}$...	$-0.760^{+0.084}_{-0.082}$	$-0.79^{+0.28}_{-0.30}$	5.65	
SNe+BAO+CMB+ H_0^{TRGB}	39.1 (34)	$0.674^{+0.007}_{-0.007}$	$0.313^{+0.007}_{-0.007}$...	$-0.805^{+0.079}_{-0.077}$	$-0.69^{+0.27}_{-0.29}$	6.20	
SNe+BAO+CMB+ $H_0^{\text{Ceph.}}$	64.7 (34)	$0.698^{+0.006}_{-0.006}$	$0.291^{+0.006}_{-0.005}$...	$-0.984^{+0.068}_{-0.066}$	$-0.30^{+0.24}_{-0.26}$	8.02	
Open w_0 - w_a								
SNe+CMB	24.5 (18)	$0.565^{+0.072}_{-0.040}$	$0.448^{+0.070}_{-0.096}$	$-0.045^{+0.031}_{-0.020}$	$-0.518^{+0.351}_{-0.269}$	$-4.75^{+3.02}_{-3.88}$
BAO+CMB	7.4 (11)	$0.652^{+0.022}_{-0.021}$	$0.337^{+0.023}_{-0.022}$	$0.001^{+0.002}_{-0.002}$	$-0.599^{+0.249}_{-0.231}$	$-1.19^{+0.68}_{-0.76}$
SNe+BAO+ ω_b	34.8 (30)	$0.670^{+0.018}_{-0.017}$	$0.321^{+0.017}_{-0.018}$	$0.004^{+0.049}_{-0.048}$	$-0.774^{+0.105}_{-0.101}$	$-0.80^{+0.54}_{-0.57}$	1.57	
SNe+BAO+CMB	34.9 (32)	$0.671^{+0.008}_{-0.008}$	$0.318^{+0.008}_{-0.008}$	$0.001^{+0.001}_{-0.001}$	$-0.787^{+0.089}_{-0.087}$	$-0.68^{+0.31}_{-0.32}$	5.23	
SNe+BAO+CMB+ H_0^{TRGB}	37.7 (33)	$0.676^{+0.008}_{-0.008}$	$0.313^{+0.007}_{-0.007}$	$0.002^{+0.001}_{-0.001}$	$-0.834^{+0.083}_{-0.082}$	$-0.57^{+0.29}_{-0.31}$	5.74	
SNe+BAO+CMB+ $H_0^{\text{Ceph.}}$	60.7 (33)	$0.701^{+0.006}_{-0.006}$	$0.292^{+0.006}_{-0.005}$	$0.003^{+0.001}_{-0.001}$	$-1.023^{+0.072}_{-0.070}$	$-0.11^{+0.27}_{-0.28}$	7.34	

Table 3. Constraints on cosmological parameters. The SN χ^2 values are based on spline-interpolated distances (with 22 nodes, so SN DoF = $22 - N_{\text{fit}}$), so they are much smaller than the number of SNe (2085). As discussed in the text, the only major tension we see between data combinations is with the Cepheid-based H_0 measurement (i.e., the “Hubble tension”); generally the probes are consistent with each other. This table also shows mild tension with flat Λ CDM, with flat w_0 - w_a reducing the SN+BAO+CMB χ^2 by 9.6.

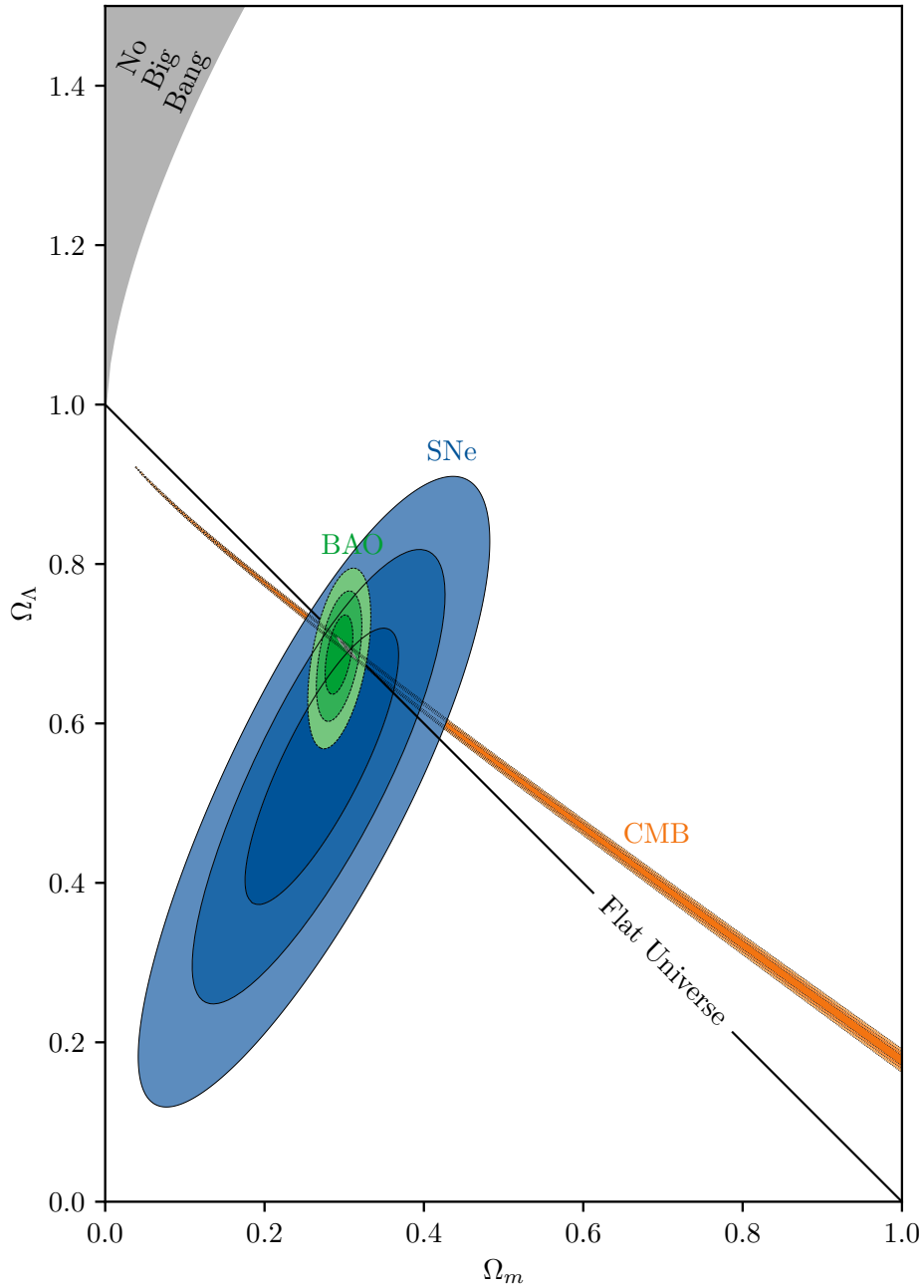


Figure 12. Constraints in the Ω_m - Ω_Λ plane. We show the constraints for SNe (in blue), BAO (in green), CMB (in orange), and combined (in gray). The probe constraints have different orientations; combining especially BAO and CMB makes for a much stronger constraint than either alone.

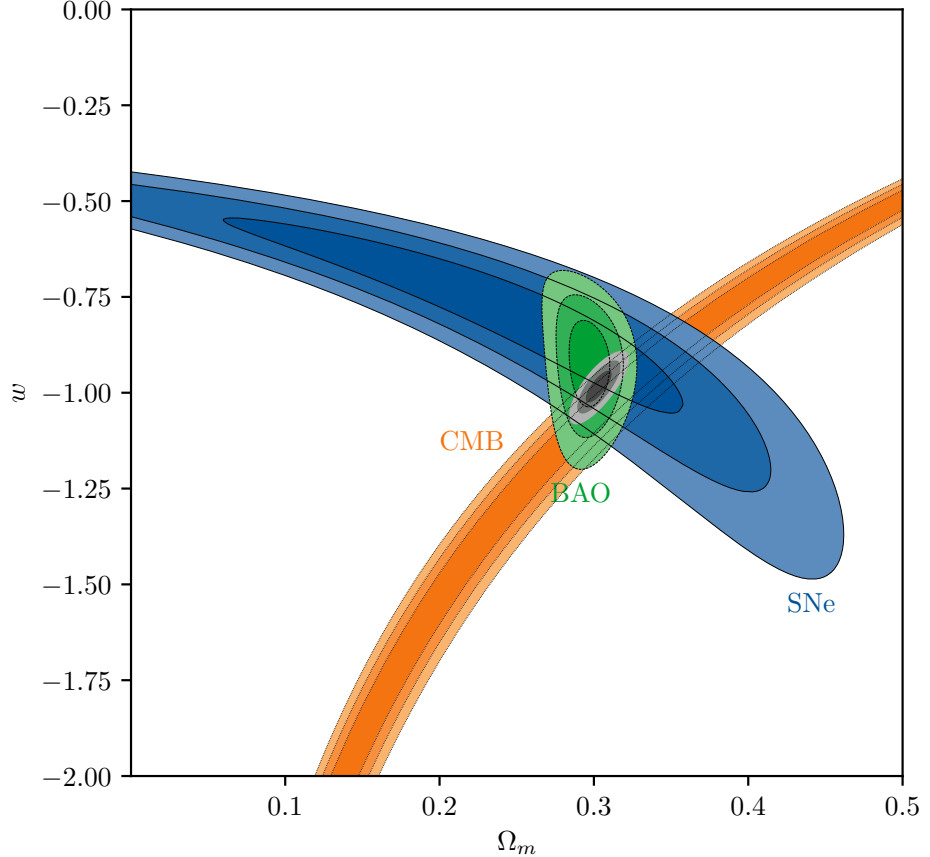


Figure 13. Constraints in the Ω_m - w plane for flat-universe, constant equation-of-state parameter w models. Again we show the constraints for SNe (in blue), BAO (in green), CMB (in orange), and combined (in gray). The probe constraints have different orientations and thus combine together for a much stronger net measurement.

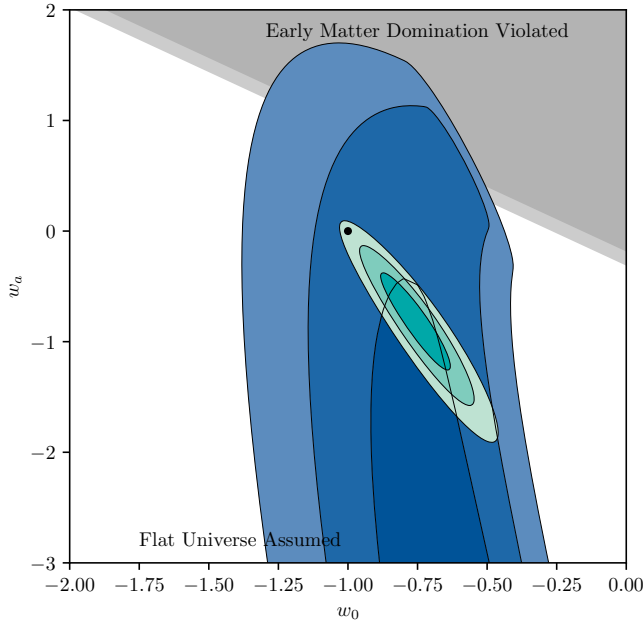


Figure 14. Constraints in the w_0 - w_a plane for flat-universe. Again we show the constraints for SNe (in blue), but now show SNe+BAO+CMB combined in teal. The SN-only constraints are consistent with the combined constraints. We indicate Λ CDM with a black dot.

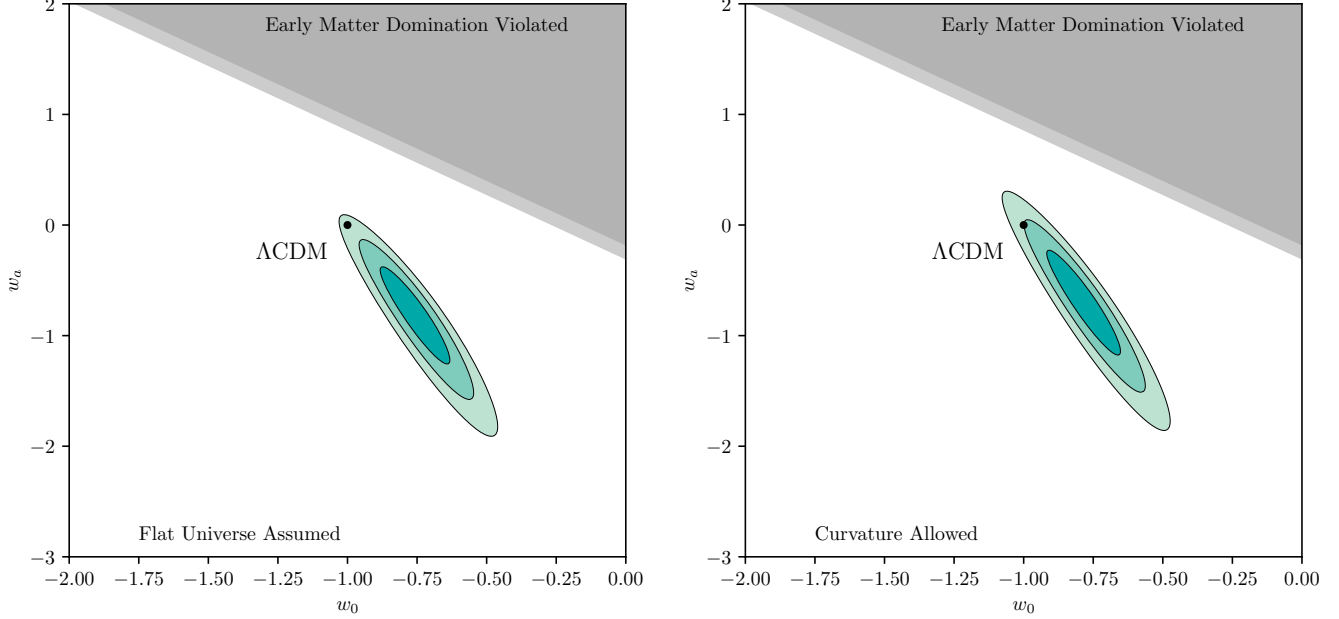


Figure 15. Constraints in the w_0 - w_a plane combining SNe, BAO, and CMB. The **left panel** shows the 1, 2, and 3σ contours assuming a flat universe, while the **right panel** also fits for curvature. We also mark off the parameter space where early matter domination would begin to be violated (the shaded regions show 1% and 10% of the matter density at $z = 1100$ assuming $\Omega_m = 0.3$). The contours show weak tension with Λ CDM (indicated with a black dot).

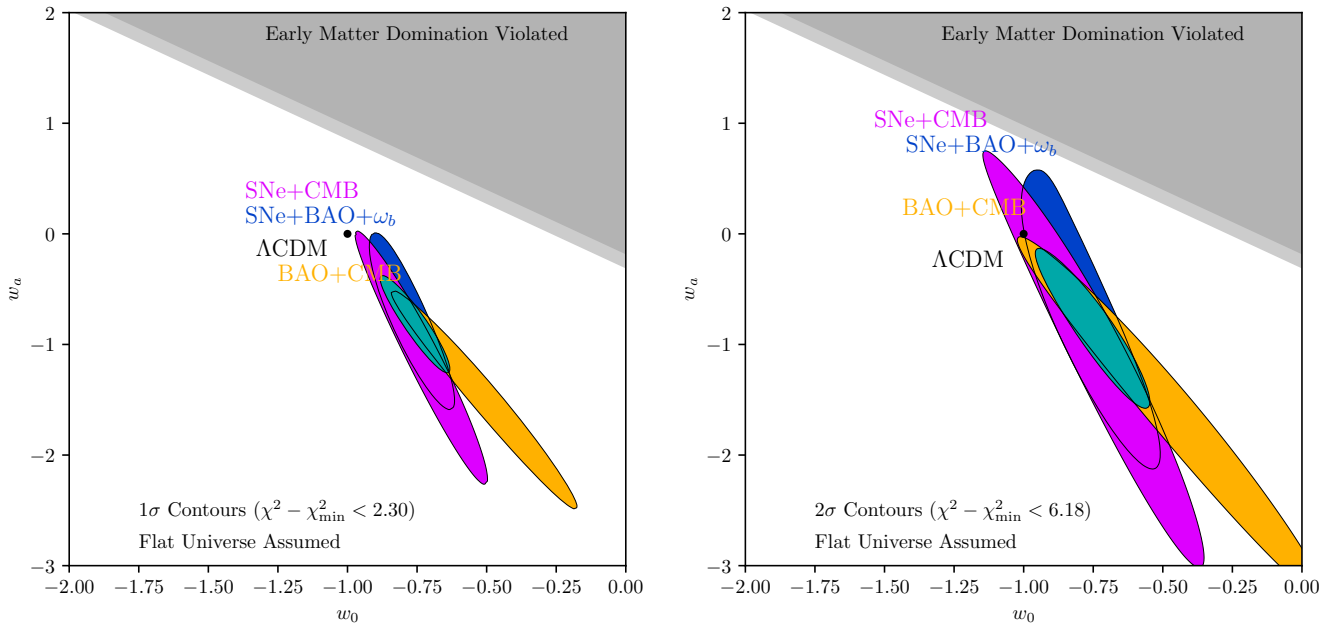


Figure 16. Constraints in the w_0 - w_a plane. The **left panel** shows the 1σ contours and the right panel shows 2σ contours, both assuming a flat universe. The contours show constraints from BAO+CMB, SNe+CMB, and SNe+BAO (as well as the same BAO+CMB+SNe contour from Figure 15). Once again, we indicate Λ CDM with a black dot. The contour for each pair of probes is angled differently, showing how the constraints get stronger when all three probes are combined together. The results from each pair of probes are compatible with the results that use all three.

In short, our most notable finding is that we continue to see mild evidence for time-varying dark energy as parameterized with the w_0 - w_a model. In fact, we find central values similar to Union3 (which used SDSS+BOSS+eBOSS BAO + 6dF), with the mild SN update towards Λ CDM ($w_0 = -1$, $w_a = 0$) canceled by the DESI move away from Λ CDM (DESI Collaboration et al. 2025). However, our uncertainties are smaller, mostly due to the DESI improvement over earlier BAO measurements. Evaluating this tension with the 2D χ^2 values (for w_0/w_a), we find an increase from 2.1σ ($\Delta\chi^2 = 6.8$) to 2.6σ ($\Delta\chi^2 = 9.6$) when including SN constraints. When also including TRGB-calibrated H_0 , the significance falls slightly to 2.2σ ($\Delta\chi^2 = 7.4$). As seen in other analyses, the Cepheid calibrated H_0 measurements have severe tension with the early universe measurements for all cosmological models considered.

5.2.1. Impact of CMB Choice on Results

Our nominal result finds somewhat lower evidence for time-evolving dark energy than, e.g., the DESI results (3.8σ for Union3+BAO+CMB, DESI Collaboration et al. 2025). Some of this difference is due to the assumed CMB constraints. As described in Rubin et al. (2025), we make our own CMB compression⁸ based on a chain from Planck PR3 (base_w_plikHM_TTTEEE_lowl_lowE, Planck Collaboration et al. 2020), which uses the `Plik` temperature (TT), polarization (EE) and cross (TE) power spectra (for $\ell \geq 30$) combined with `SimAll+Commander` (for $\ell < 30$). In contrast, DESI retains `SimAll+Commander` (for $\ell < 30$) but combines with `CamSpec` for $\ell \geq 30$ (Rosenberg et al. 2022), and also includes Planck and ACT DR6 CMB lensing (Madhavacheril et al. 2024). DESI also uses the full CMB likelihood.

Table 4 presents the range of significance against a cosmological constant under the w_0 - w_a parametrization. The table is broken into three blocks for three major Union+UNITY releases, Union3+UNITY1.5 (Rubin et al. 2025), Union3.1+UNITY1.7 (Hoyt et al. 2026), and Union3.1+UNITY1.8 (this work). Comparing the top row of the topmost block, based on the older Union3+UNITY1.5 SN measurements, with the other two rows of the same block emphasizes the impact of the new DESI-DR2 BAO measurements on increasing tension with Λ CDM. The bottom two rows of all three blocks in the table use the exact same assumptions and methodologies, allowing us to trace directly the impact of

⁸ In other words, replacing the full CMB likelihood with a constraint on the shift parameter, angular scale, and baryon density $\{R, \theta_*, \Omega_b h^2\}$.

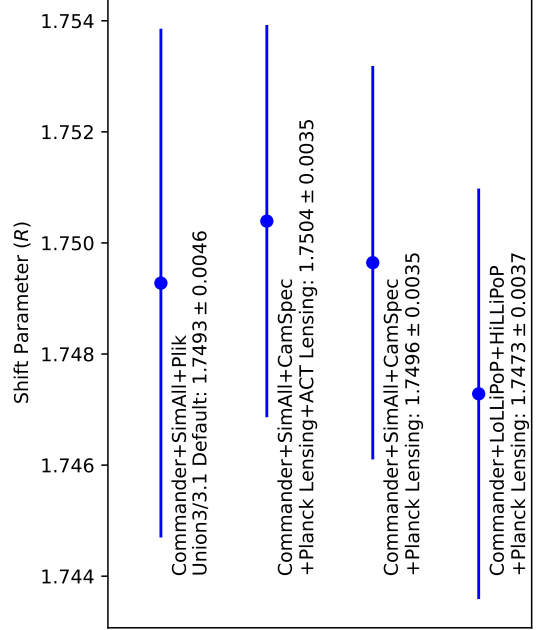


Figure 17. Comparison of our shift-parameter measurements derived from MCMC chains. The choice of CMB likelihood and data has an impact on the inferred shift parameter with a peak-to-peak range close to the quoted uncertainties.

the different SN measurements on w_0 - w_a constraints. Going from Union3+UNITY1.5 to Union3.1 and either UNITY1.7 or UNITY1.8 decreases tension against a cosmological constant by 0.4σ and 0.5σ , respectively. In the last block, we explore a broader range of CMB assumptions, comparing `Commander+SimAll+CamSpec` with `Commander+LoLLiPop` (Tristram et al. 2021) +`HiLLiPop` (Tristram et al. 2024), both with Planck PR4 lensing; this difference is 0.3σ on the level of tension.⁹ Figure 17 shows that there are significant differences (comparable to the quoted uncertainties) in the inferred shift parameter values for these combinations.

6. CONCLUSIONS

⁹ When making compressed likelihoods, we generated `Cobaya` (Torrado & Lewis 2021) input files using the online input generator: <https://cobaya-gui.streamlit.app> for `CAMB` (Lewis & Challinor 2011), except for the DESI combination (`Commander+SimAll+CamSpec`, Planck and ACT DR6 CMB lensing), where we used DESI’s input file. We ran each chain until the Gelman & Rubin (1992) \hat{R} statistic was below 1.005. We discarded the first 30% of the chain as burn in and computed $\{R, \theta_*, \Omega_b h^2\}$ for each MCMC sample, taking each sample’s weight into account.

Table 4. Table showing how different SN and CMB analyses impact the observed deviations from a cosmological constant in the w_0 - w_a plane.

BAO	CMB					Reference
	Planck Likelihoods	Lensing	Treatment	Significance		
Union3+UNITY1.5						
6dF+SDSS+ BOSS+eBOSS	Commander+SimAll (low- ℓ) Plik (high- ℓ)	No lensing	Compressed $\{R, \theta_*, \Omega_b h^2\}$	$\Delta\chi^2 = 7.3, 2.2\sigma$	Rubin et al. (2025)	
DESI-DR2 +6dF	Commander+SimAll (low- ℓ) CamSpecNPIPE (high- ℓ)	Planck+ ACT-DR6	Compressed $\{R, \theta_*, \Omega_b h^2\}$	$\Delta\chi^2 = 15.6, 3.5\sigma$	This Work	
DESI-DR2	Commander+SimAll (low- ℓ) CamSpecNPIPE (high- ℓ)	Planck+ ACT-DR6	Full	$\Delta\chi^2 = 17.4, 3.8\sigma$	DESI Collaboration et al. (2025)	
Union3.1+UNITY1.7						
DESI-DR2 +6dF	Commander+SimAll (low- ℓ) CamSpecNPIPE (high- ℓ)	Planck+ ACT-DR6	Compressed $\{R, \theta_*, \Omega_b h^2\}$	$\Delta\chi^2 = 12.4, 3.1\sigma$	This Work	
DESI-DR2 ^a	Commander+SimAll (low- ℓ) CamSpecNPIPE (high- ℓ)	Planck+ ACT-DR6	Full	$\Delta\chi^2 = 14.4, 3.4\sigma$	Hoyt et al. (2026)	
Union3.1+UNITY1.8						
DESI-DR2 +6dF	Commander+SimAll (low- ℓ) Plik (high- ℓ)	No lensing	Compressed $\{R, \theta_*, \Omega_b h^2\}$	$\Delta\chi^2 = 9.6, 2.6\sigma$	This Work	
DESI-DR2 +6dF	Commander+LoLLiPoP (low- ℓ) HiLLiPoP (high- ℓ)	Planck PR4	Compressed $\{R, \theta_*, \Omega_b h^2\}$	$\Delta\chi^2 = 9.4, 2.6\sigma$	This Work	
sDESI-DR2 +6dF	Commander+SimAll (low- ℓ) CamSpecNPIPE (high- ℓ)	Planck PR4	Compressed $\{R, \theta_*, \Omega_b h^2\}$	$\Delta\chi^2 = 11.3, 2.9\sigma$	This Work	
DESI-DR2 +6dF	Commander+SimAll (low- ℓ) CamSpecNPIPE (high- ℓ)	Planck+ ACT-DR6	Compressed $\{R, \theta_*, \Omega_b h^2\}$	$\Delta\chi^2 = 12.0, 3.0\sigma$	This Work	
DESI-DR2 ^a	Commander+SimAll (low- ℓ) CamSpecNPIPE (high- ℓ)	Planck+ ACT-DR6	Full	$\Delta\chi^2 = 14.0, 3.3\sigma$	Hoyt et al. (2026)	

NOTE—Each section of the table combines a different version of the Union+UNITY SN cosmology analysis with BAO measurements and different, comparably valid choices for the adopted Planck CMB likelihood such as the treatment of noise in the maps. Note that 6dF is a very low redshift BAO point and has a small effect on inferred cosmological parameters because SNe dominate the constraining power at low redshifts.

^aHigh redshift datasets, assumptions, and methods adopted exactly as per the nominal BAO+CMB+SN analysis of DESI Collaboration et al. (2025). Comparing with their published result (topmost block of table) directly traces the impact that the new Union+UNITY SN analyses have on their reported w_0 - w_a tension with Λ CDM.

This work introduces UNITY1.8, a Bayesian hierarchical model that incorporates two modes of normal SNe Ia. Each SN is only probabilistically assigned to each mode, and the relative fractions are fit for and allowed to vary in redshift and host-galaxy stellar-mass bins. The two modes have separate absolute magnitudes, x_1 and “intrinsic” (assumed Gaussian distributed) color distributions, and x_1 standardization coefficients.

Using tests with the predictive posterior distributions, we show evidence that UNITY1.8 matches the

data better than older, single-mode UNITY models. In simulated-data testing, we do find small (~ 0.1 in x_1) Eddington-like biases on x_1 population parameters. However the x_1 population parameters were $\sim 1\%$ of the total cosmological-uncertainty variance in Union3 and we see no evidence of bias on cosmological parameters, so we consider this acceptable.

Encouragingly, we find that UNITY1.8 makes the host-stellar-mass/luminosity step consistent with zero for unreddened SNe. The only remaining host-stellar-

mass dependence is in the color-standardization coefficient of red SNe (β_R).

We find very low unexplained dispersions for the slow-mode SNe from mid-redshift SN datasets that have rolling light curves and scene-modeling photometry. Whether this is an artifact of SALT3 (e.g., an overestimated uncertainty model), or whether it is an intrinsic property of SNe Ia will need further investigation.

We find UNITY1.8 decreases the cosmological-parameter uncertainties compared to earlier models. We still see some tension with flat Λ CDM, finding mild evidence for time-varying dark energy models. The strength of this tension is dependent on the choice of CMB likelihood and how it is treated, varying from 2.6σ to 3.3σ .

Finally, we find it strongly encouraging that a substantially different standardization two-population model yields consistent cosmological constraints with prior work that assumed a single population.

¹ We thank Paul Shah and Andrei Cuceu for discussions of CMB constraints. This research uses services or data provided by the Astro Data Lab, which is part of the Community Science and Data Center (CSDC) Program of NSF NOIRLab. NOIRLab is operated by the Association of Universities for Research in Astronomy (AURA), Inc. under a cooperative agreement with the U.S. National Science Foundation. The technical support and advanced computing resources from University of Hawai‘i Information Technology Services - Research Cyberinfrastructure, funded in part by the National Science Foundation CC* awards #2201428 and #2232862 are gratefully acknowledged. Support for this work was provided by NASA through grant number HST-AR-16631.001-A from the Space Telescope Science Institute, which is operated by AURA, Inc., under NASA contract NAS 5-26555. This work was supported in part by the Director, Office of Science, Office of High Energy Physics of the U.S. Department of Energy under Contract No. DE-AC02-05CH11231.

Software: Astropy (Astropy Collaboration 2013), CAMB (Lewis & Challinor 2011), Cobaya (Torrado & Lewis 2021), Extinction (Barbary 2016), Matplotlib (Hunter 2007), Numpy (van der Walt et al. 2011), PairV (Davis et al. 2011), PyStan (Riddell et al. 2018), SciPy (Jones et al. 2001), SNCosmo (Barbary et al. 2016), Stan (Carpenter et al. 2017)

APPENDIX

A. SIMULATED-DATA TESTING

Simulated-data testing is an essential part of a complex analysis to ensure the correctness of the results. As noted above, we performed our simulated-data testing before unblinding the cosmological parameters from the real data. Our simulated-data testing is based on that done for Union3+UNITY1.5 (Rubin et al. 2025) with a few differences. In short, this testing simulated different rolling-survey datasets: one at very low redshift similar to the Lick Observatory Supernova Search SNe (Ganeshalingam et al. 2010), one at low redshift similar to Foundation (Foley et al. 2018), one at mid redshift similar to the Dark Energy Survey deep tier (Dark Energy Survey Collaboration et al. 2016) with 600 SNe, and one at high redshift similar to the Multi-Cycle Treasury programs (Riess et al. 2018) with an average of 78 SNe after selection cuts. The high-redshift dataset was purely magnitude limited (as assumed by UNITY), but the others had a simulated spectroscopic observer who picked out the brightest SNe available to observe on a given date. This makes for a more difficult (but realistic) test for UNITY. The updates are the following:

- To improve the realism now that UNITY will be used for Hubble-constant measurements, we now simulate two magnitude-limited nearby datasets, one in *griz* filters with a depth of 20 AB at 5σ in all filters (the same as in Union3), but also another one with a depth of 19 AB and light curves in *BVRI* filters. As can be seen in Tables 5 and 6, after simulated spectroscopic selection, this dataset is about 1.5 magnitudes shallower.
- For both nearby datasets, we simulate 300 Hubble-flow SNe and 20 calibrator SNe. These calibrators have a simple distance-ladder covariance matrix of (0.05 magnitudes)² along the diagonal and (0.02 magnitudes)² zeropoint uncertainty shared among all entries; these values are roughly similar to Riess et al. 2022. We also assume a mean host stellar mass of 10.4 ± 1 (not 10 ± 1) for the calibrator SNe to make sure that we can standardize across different host-galaxy selections as will be required for the Hubble constant.
- We simulate from a two- x_1 -mode model with parameters given in Tables 5 and 6, which are similar to the values found for the real data (Section 4). This enables a test of UNITY1.8, but also shows us what happens when UNITY1.7 runs on data simulated assuming a two-mode model.
- A minor change from the Union3+UNITY1.5 testing is the inclusion of photometric uncertainties in the magnitudes used for spectroscopic selection. This was left out of the old testing to be a harder test for UNITY1.5 to pass. The bias due to selection effects scales as (corrected Hubble dispersion)²/(uncorrected dispersion), and if the photometric uncertainties are included in the selection, they are added in quadrature to the denominator. So sharp cuts in magnitude mean worse selection effect biases than are generally present in the real data.

Similarly to the testing in Union3, we perform a realistic test and do not test UNITY with data simulated from UNITY. For example, the simulated data generation simulates an observer who selects bright SNe to spectroscopically confirm, but UNITY models selection as an error function in magnitude. The simulated data assumes an exponential distribution of red color c_R^{true} , but UNITY approximates this with a mixture of four Gaussians (Rubin et al. 2025, Appendix C).

Table 5 shows the results of our simulated-data testing assuming flat Λ CDM and Table 6 shows the results assuming flat w_0-w_a (with Ω_m fixed). Each row is a parameter in the analysis while the columns compare the performance of UNITY1.8 (our new recommended analysis) and UNITY1.7. For each of the 100 realizations, for each UNITY parameter, we compute the posterior median (as an estimate of the best-fit value) and one half the difference between the 84.1st percentile and the 15.9th percentile as an estimate of the uncertainty. Then, for each UNITY parameter, we quote (up to) four numbers in the table. The first is the mean of the best-fit values. The second is the mean of the uncertainties. In the parentheses, we quote the mean of the pulls, the mean best fit minus the mean true value divided by the mean uncertainty. For the parameters where we do see a bias, this gives a sense of how significant the bias is as a fraction of the uncertainty. The second number in the parentheses is the uncertainty on the mean pull. In other words, it is the RMS of the best-fit values divided by $\sqrt{N^{\text{realizations}}} = 10$ divided by the mean uncertainty. For Gaussian-distributed parameters with correctly estimated uncertainties and 100 realizations, this should be 0.1σ . Note that the true value does not have to exist in order to compute the uncertainty on the mean pull, i.e., a single

α value does not exist in the simulations, but one can still ask if UNITY1.7 recovers a consistent α value (within uncertainties) across the 100 realizations.

B. BAO RESULTS

Table 7 presents the BAO distances used in this work. We standardize the sound horizon (r_d) values to the assumptions used in the cosmology analysis following Rubin et al. (2025). In short, BAO distances are measured with respect to the sound horizon:

$$r_d = \int_{z_d}^{\infty} \frac{c_s(z') dz'}{H(z')} . \quad (\text{B1})$$

Unfortunately, different approximations can scale r_d by a cosmology-independent constant and different results are quoted relative to different fiducial cosmologies. Denoting r_d^{ours} to be r_d using our approximations (described in more detail in Rubin et al. 2025), we rescale all BAO measurements to be on a consistent scale. For example, for the DESI BGS measurement, we write

$$D_V(z_{\text{eff}} = 0.295) \left[\frac{r_{d,\text{fid}}^{\text{ours}}}{r_d^{\text{ours}}} \right] = 1168.189 \pm 11.032 \text{ Mpc} .$$

where $r_{d,\text{fid}}^{\text{ours}}$ has to be computed for the same cosmological parameters as each BAO analysis used to compute their $r_{d,\text{fid}}$.

Parameter	Input	UNITY1.8, Two- x_1 Modes	UNITY1.7
Cosmology Parameters			
H_0	71.000	$70.864 \pm 1.017 (-0.13 \pm 0.10)\sigma$	$71.006 \pm 1.037 (+0.01 \pm 0.09)\sigma$
Ω_m	0.300	$0.304 \pm 0.017 (+0.23 \pm 0.08)\sigma$	$0.313 \pm 0.020 (+0.69 \pm 0.08)\sigma$
Standardization Parameters			
α	$0.158 \pm 0.011 (\cdots \pm 0.14)\sigma$
α slow	0.170	$0.141 \pm 0.023 (-1.30 \pm 0.13)\sigma$...
α fast – slow	0.070	$0.068 \pm 0.023 (-0.09 \pm 0.11)\sigma$...
\mathcal{M}_B fast – slow	0.180	$0.159 \pm 0.024 (-0.88 \pm 0.09)\sigma$...
β_B	2.100	$2.074 \pm 0.238 (-0.11 \pm 0.10)\sigma$	$2.062 \pm 0.247 (-0.15 \pm 0.11)\sigma$
β_{RL}	4.400	$4.427 \pm 0.190 (+0.14 \pm 0.09)\sigma$	$4.200 \pm 0.188 (-1.06 \pm 0.09)\sigma$
β_{RH}	3.200	$3.247 \pm 0.199 (+0.24 \pm 0.09)\sigma$	$3.334 \pm 0.255 (+0.53 \pm 0.10)\sigma$
$\delta(z = 0)$	0.000	$-0.006 \pm 0.015 (-0.42 \pm 0.09)\sigma$	$0.024 \pm 0.015 (+1.54 \pm 0.08)\sigma$
$\delta(z = \infty)/\delta(z = 0)$	$\mathcal{U}(0, 1)$	$0.428 \pm 0.262 (-0.26 \pm 0.07)\sigma$	$0.426 \pm 0.284 (-0.25 \pm 0.05)\sigma$
step mass	10.000	$10.000 \pm 0.064 (-0.00 \pm 0.12)\sigma$	$9.997 \pm 0.069 (-0.05 \pm 0.11)\sigma$
Population Parameters			
x_1^* Fast	-0.900	$-0.765 \pm 0.114 (+1.18 \pm 0.10)\sigma$...
R^{x_1} Fast	0.800	$0.909 \pm 0.072 (+1.51 \pm 0.10)\sigma$...
x_1^* Slow	0.500	$0.496 \pm 0.038 (-0.10 \pm 0.10)\sigma$...
R^{x_1} Slow	0.500	$0.544 \pm 0.046 (+0.98 \pm 0.14)\sigma$...
c^* Fast	-0.050	$-0.049 \pm 0.008 (+0.06 \pm 0.09)\sigma$...
R^c Fast	0.060	$0.061 \pm 0.006 (+0.12 \pm 0.10)\sigma$...
c^* Slow	-0.080	$-0.078 \pm 0.005 (+0.42 \pm 0.10)\sigma$...
R^c Slow	0.040	$0.041 \pm 0.003 (+0.24 \pm 0.11)\sigma$...
m_{50} Very Low- z	...	$16.187 \pm 0.090 (\cdots \pm 0.12)\sigma$	$16.192 \pm 0.090 (\cdots \pm 0.12)\sigma$
σ_m Very Low- z	...	$0.246 \pm 0.040 (\cdots \pm 0.14)\sigma$	$0.248 \pm 0.041 (\cdots \pm 0.14)\sigma$
σ^{unexpl} Very Low- z	0.080	$0.068 \pm 0.017 (-0.69 \pm 0.10)\sigma$	$0.105 \pm 0.011 (+2.22 \pm 0.11)\sigma$
m_{50} Low- z	...	$17.650 \pm 0.103 (\cdots \pm 0.09)\sigma$	$17.649 \pm 0.104 (\cdots \pm 0.10)\sigma$
σ_m Low- z	...	$0.273 \pm 0.046 (\cdots \pm 0.14)\sigma$	$0.275 \pm 0.046 (\cdots \pm 0.14)\sigma$
σ^{unexpl} Low- z	0.080	$0.069 \pm 0.013 (-0.82 \pm 0.11)\sigma$	$0.101 \pm 0.009 (+2.21 \pm 0.12)\sigma$
m_{50} Mid- z	...	$23.134 \pm 0.058 (\cdots \pm 0.11)\sigma$	$23.136 \pm 0.059 (\cdots \pm 0.11)\sigma$
σ_m Mid- z	...	$0.215 \pm 0.026 (\cdots \pm 0.13)\sigma$	$0.215 \pm 0.027 (\cdots \pm 0.13)\sigma$
σ^{unexpl} Mid- z	0.080	$0.071 \pm 0.011 (-0.82 \pm 0.12)\sigma$	$0.101 \pm 0.008 (+2.66 \pm 0.11)\sigma$
m_{50} High- z	...	$25.984 \pm 0.228 (\cdots \pm 0.06)\sigma$	$25.984 \pm 0.233 (\cdots \pm 0.06)\sigma$
σ_m High- z	...	$0.303 \pm 0.143 (\cdots \pm 0.04)\sigma$	$0.306 \pm 0.144 (\cdots \pm 0.04)\sigma$
σ^{unexpl} High- z	0.080	$0.066 \pm 0.031 (-0.44 \pm 0.08)\sigma$	$0.097 \pm 0.028 (+0.63 \pm 0.10)\sigma$
σ^{unexpl} fast	0.080	$0.098 \pm 0.018 (+0.98 \pm 0.10)\sigma$...
f^{m_B}	Simplex	$0.472 \pm 0.236 (+0.64 \pm 0.05)\sigma$	$0.468 \pm 0.162 (+0.90 \pm 0.10)\sigma$
f^{x_1}	Simplex	$0.230 \pm 0.155 (-0.86 \pm 0.07)\sigma$	$0.291 \pm 0.090 (-0.79 \pm 0.16)\sigma$
f^c	Simplex	$0.254 \pm 0.188 (-0.33 \pm 0.06)\sigma$	$0.225 \pm 0.157 (-0.58 \pm 0.07)\sigma$
f^{outl}	0.008–0.029	$0.012 \pm 0.003 (-2.09 \pm 0.09)\sigma$	$0.015 \pm 0.004 (-0.93 \pm 0.09)\sigma$

Table 5. Simulated-data results assuming flat Λ CDM. We show results for both UNITY1.8 and UNITY1.7, run on the same set of input simulations. As described in the text, we show (up to) four numbers for each parameter, for each UNITY model. The first is the mean of the best-fit values, the second is the mean uncertainty over the 100 realizations. In parentheses, we show the mean pull and the uncertainty on the mean pull.

Parameter	Input	UNITY1.8, Two- x_1 Modes	UNITY1.7
Cosmology Parameters			
H_0	71.000	$70.870 \pm 1.030 (-0.13 \pm 0.09)\sigma$	$71.085 \pm 1.050 (+0.08 \pm 0.09)\sigma$
w_0	-1.000	$-0.993 \pm 0.119 (+0.06 \pm 0.09)\sigma$	$-1.034 \pm 0.123 (-0.28 \pm 0.09)\sigma$
$w_0 + 0.15 w_a$	-1.000	$-0.999 \pm 0.048 (+0.02 \pm 0.08)\sigma$	$-0.982 \pm 0.053 (+0.35 \pm 0.09)\sigma$
w_a	0.000	$-0.029 \pm 0.735 (-0.04 \pm 0.09)\sigma$	$0.367 \pm 0.738 (+0.50 \pm 0.08)\sigma$
Standardization Parameters			
α	$0.158 \pm 0.011 (\cdots \pm 0.14)\sigma$
α slow	0.170	$0.140 \pm 0.022 (-1.34 \pm 0.13)\sigma$...
α fast – slow	0.070	$0.067 \pm 0.022 (-0.13 \pm 0.11)\sigma$...
\mathcal{M}_B fast – slow	0.180	$0.159 \pm 0.024 (-0.88 \pm 0.09)\sigma$...
β_B	2.100	$2.073 \pm 0.239 (-0.11 \pm 0.10)\sigma$	$2.065 \pm 0.249 (-0.14 \pm 0.11)\sigma$
β_{RL}	4.400	$4.433 \pm 0.190 (+0.17 \pm 0.09)\sigma$	$4.204 \pm 0.188 (-1.04 \pm 0.09)\sigma$
β_{RH}	3.200	$3.253 \pm 0.199 (+0.27 \pm 0.09)\sigma$	$3.336 \pm 0.247 (+0.55 \pm 0.10)\sigma$
$\delta(z = 0)$	0.000	$-0.007 \pm 0.015 (-0.44 \pm 0.09)\sigma$	$0.023 \pm 0.015 (+1.53 \pm 0.08)\sigma$
$\delta(z = \infty)/\delta(z = 0)$	$\mathcal{U}(0, 1)$	$0.433 \pm 0.264 (-0.24 \pm 0.07)\sigma$	$0.438 \pm 0.287 (-0.20 \pm 0.05)\sigma$
step mass	10.000	$9.998 \pm 0.065 (-0.03 \pm 0.12)\sigma$	$9.997 \pm 0.069 (-0.04 \pm 0.12)\sigma$
Population Parameters			
x_1^* Fast	-0.900	$-0.766 \pm 0.114 (+1.18 \pm 0.10)\sigma$...
R^{x_1} Fast	0.800	$0.913 \pm 0.072 (+1.56 \pm 0.10)\sigma$...
x_1^* Slow	0.500	$0.496 \pm 0.038 (-0.10 \pm 0.10)\sigma$...
R^{x_1} Slow	0.500	$0.546 \pm 0.045 (+1.02 \pm 0.14)\sigma$...
c^* Fast	-0.050	$-0.049 \pm 0.008 (+0.09 \pm 0.09)\sigma$...
R^c Fast	0.060	$0.061 \pm 0.006 (+0.14 \pm 0.10)\sigma$...
c^* Slow	-0.080	$-0.078 \pm 0.005 (+0.43 \pm 0.10)\sigma$...
R^c Slow	0.040	$0.041 \pm 0.003 (+0.27 \pm 0.11)\sigma$...
m_{50} Very Low- z	...	$16.189 \pm 0.091 (\cdots \pm 0.12)\sigma$	$16.197 \pm 0.089 (\cdots \pm 0.12)\sigma$
σ_m Very Low- z	...	$0.246 \pm 0.041 (\cdots \pm 0.14)\sigma$	$0.247 \pm 0.041 (\cdots \pm 0.14)\sigma$
σ^{unexpl} Very Low- z	0.080	$0.068 \pm 0.017 (-0.70 \pm 0.10)\sigma$	$0.105 \pm 0.011 (+2.19 \pm 0.11)\sigma$
m_{50} Low- z	...	$17.652 \pm 0.103 (\cdots \pm 0.09)\sigma$	$17.652 \pm 0.103 (\cdots \pm 0.10)\sigma$
σ_m Low- z	...	$0.273 \pm 0.046 (\cdots \pm 0.14)\sigma$	$0.275 \pm 0.046 (\cdots \pm 0.14)\sigma$
σ^{unexpl} Low- z	0.080	$0.069 \pm 0.013 (-0.86 \pm 0.11)\sigma$	$0.101 \pm 0.009 (+2.18 \pm 0.12)\sigma$
m_{50} Mid- z	...	$23.132 \pm 0.059 (\cdots \pm 0.11)\sigma$	$23.135 \pm 0.060 (\cdots \pm 0.11)\sigma$
σ_m Mid- z	...	$0.215 \pm 0.026 (\cdots \pm 0.13)\sigma$	$0.216 \pm 0.027 (\cdots \pm 0.13)\sigma$
σ^{unexpl} Mid- z	0.080	$0.071 \pm 0.011 (-0.81 \pm 0.12)\sigma$	$0.102 \pm 0.008 (+2.68 \pm 0.11)\sigma$
m_{50} High- z	...	$25.984 \pm 0.234 (\cdots \pm 0.06)\sigma$	$25.997 \pm 0.235 (\cdots \pm 0.06)\sigma$
σ_m High- z	...	$0.305 \pm 0.144 (\cdots \pm 0.04)\sigma$	$0.304 \pm 0.146 (\cdots \pm 0.04)\sigma$
σ^{unexpl} High- z	0.080	$0.066 \pm 0.031 (-0.44 \pm 0.08)\sigma$	$0.097 \pm 0.028 (+0.62 \pm 0.10)\sigma$
σ^{unexpl} fast	0.080	$0.098 \pm 0.018 (+0.97 \pm 0.10)\sigma$...
f^{m_B}	Simplex	$0.486 \pm 0.237 (+0.69 \pm 0.06)\sigma$	$0.462 \pm 0.160 (+0.88 \pm 0.10)\sigma$
f^{x_1}	Simplex	$0.223 \pm 0.155 (-0.90 \pm 0.07)\sigma$	$0.295 \pm 0.091 (-0.75 \pm 0.16)\sigma$
f^c	Simplex	$0.247 \pm 0.188 (-0.36 \pm 0.06)\sigma$	$0.226 \pm 0.158 (-0.56 \pm 0.07)\sigma$
f^{outl}	0.008–0.029	$0.012 \pm 0.003 (-2.07 \pm 0.09)\sigma$	$0.015 \pm 0.004 (-0.93 \pm 0.10)\sigma$

Table 6. Simulated-data results assuming flat w_0 – w_a . We show results for both UNITY1.8 and UNITY1.7, run on the same set of input simulations. As described in the text, we show (up to) four numbers for each parameter, for each UNITY model. The first is the mean of the best-fit values, the second is the mean uncertainty over the 100 realizations. In parentheses, we show the mean pull and the uncertainty on the mean pull.

Measurement	Type	z	Our r_d	Distance	Covariance Matrix						
6dF	D_V	0.106	153.745	457.574	417.279	0	0	0	0	0	0
BGS	D_V	0.295	150.617	1168.189	0	121.700	0	0	0	0	0
LRG1	D_M	0.51	150.617	1998.659	0	603.392	20.432	0	0	0	0
LRG1	H	0.51	150.617	93.224	0	0	20.432	3.284	0	0	0
LRG2	D_M	0.706	150.617	2552.159	0	0	0	677.818	18.691	0	0
LRG2	H	0.706	150.617	104.763	0	0	0	18.691	3.158	0	0
LRG3+ELG1	D_M	0.934	150.617	3173.614	0	0	0	0	499.866	11.756	0
LRG3+ELG1	H	0.934	150.617	115.535	0	0	0	0	11.756	1.598	0
ELG2	D_M	1.321	150.617	4059.831	0	0	0	0	0	2187.865	45.501
ELG2	H	1.321	150.617	143.775	0	0	0	0	45.501	5.024	0
QSO	D_M	1.484	150.617	4488.010	0	0	0	0	0	12496.646	357.834
QSO	H	1.484	150.617	159.020	0	0	0	0	0	357.834	40.985
Ly α	D_M	2.33	150.617	5734.745	0	0	0	0	0	0	6100.358
Ly α	H	2.33	150.617	236.116	0	0	0	0	0	0	93.002
											7.633

Table 7. BAO distances for this analysis. The first line is from 6dF (Beutler et al. 2011); the others are from DESI DR2 (DESI Collaboration et al. 2025).

REFERENCES

Adame, A. G., Aguilar, J., Ahlen, S., et al. 2025, *JCAP*, 2025, 021, doi: [10.1088/1475-7516/2025/02/021](https://doi.org/10.1088/1475-7516/2025/02/021)

Alam, S., Ata, M., Bailey, S., et al. 2017, *MNRAS*, 470, 2617, doi: [10.1093/mnras/stx721](https://doi.org/10.1093/mnras/stx721)

Alam, S., Aubert, M., Avila, S., et al. 2021, *PhRvD*, 103, 083533, doi: [10.1103/PhysRevD.103.083533](https://doi.org/10.1103/PhysRevD.103.083533)

Amanullah, R., Lidman, C., Rubin, D., et al. 2010, *ApJ*, 716, 712, doi: [10.1088/0004-637X/716/1/712](https://doi.org/10.1088/0004-637X/716/1/712)

Arnett, W. D. 1982, *ApJ*, 253, 785, doi: [10.1086/159681](https://doi.org/10.1086/159681)

Arnett, W. D., Branch, D., & Wheeler, J. C. 1985, *Nature*, 314, 337, doi: [10.1038/314337a0](https://doi.org/10.1038/314337a0)

Astier, P., El Hage, P., Guy, J., et al. 2013, *A&A*, 557, A55, doi: [10.1051/0004-6361/201321668](https://doi.org/10.1051/0004-6361/201321668)

Astropy Collaboration. 2013, *A&A*, 558, A33

Barbary, K. 2016, extinction v0.3.0, Zenodo, doi: [10.5281/zenodo.804967](https://doi.org/10.5281/zenodo.804967)

Barbary, K., Barclay, T., Biswas, R., et al. 2016, SNCosmo: Python library for supernova cosmology. <http://ascl.net/1611.017>

Bautista, J. E., Paviot, R., Vargas Magaña, M., et al. 2021, *MNRAS*, 500, 736, doi: [10.1093/mnras/staa2800](https://doi.org/10.1093/mnras/staa2800)

Beutler, F., Blake, C., Colless, M., et al. 2011, *MNRAS*, 416, 3017, doi: [10.1111/j.1365-2966.2011.19250.x](https://doi.org/10.1111/j.1365-2966.2011.19250.x)

Breuval, L., Riess, A. G., Casertano, S., et al. 2024, *ApJ*, 973, 30, doi: [10.3847/1538-4357/ad630e](https://doi.org/10.3847/1538-4357/ad630e)

Brout, D., & Scolnic, D. 2021, *The Astrophysical Journal*, 909, 26, doi: [10.3847/1538-4357/abd69b](https://doi.org/10.3847/1538-4357/abd69b)

Burns, C. R., Stritzinger, M., Phillips, M. M., et al. 2014, *ApJ*, 789, 32, doi: [10.1088/0004-637X/789/1/32](https://doi.org/10.1088/0004-637X/789/1/32)

Burns, C. R., Parent, E., Phillips, M. M., et al. 2018, *ApJ*, 869, 56, doi: [10.3847/1538-4357/aae51c](https://doi.org/10.3847/1538-4357/aae51c)

Carpenter, B., Gelman, A., Hoffman, M. D., et al. 2017, *Journal of Statistical Software*, 76, 1, doi: [10.18637/jss.v076.i01](https://doi.org/10.18637/jss.v076.i01)

Childress, M. J., Wolf, C., & Zahid, H. J. 2014, *MNRAS*, 445, 1898, doi: [10.1093/mnras/stu1892](https://doi.org/10.1093/mnras/stu1892)

Chotard, N., Gangler, E., Aldering, G., et al. 2011, *A&A*, 529, L4, doi: [10.1051/0004-6361/201116723](https://doi.org/10.1051/0004-6361/201116723)

Cooke, R. J., Pettini, M., Nollett, K. M., & Jorgenson, R. 2016, *ApJ*, 830, 148, doi: [10.3847/0004-637X/830/2/148](https://doi.org/10.3847/0004-637X/830/2/148)

Dark Energy Survey Collaboration, Abbott, T., Abdalla, F. B., et al. 2016, *MNRAS*, 460, 1270, doi: [10.1093/mnras/stw641](https://doi.org/10.1093/mnras/stw641)

Davis, T. M., Hui, L., Frieman, J. A., et al. 2011, *ApJ*, 741, 67, doi: [10.1088/0004-637X/741/1/67](https://doi.org/10.1088/0004-637X/741/1/67)

de Mattia, A., Ruhlmann-Kleider, V., Raichoor, A., et al. 2021, *MNRAS*, 501, 5616, doi: [10.1093/mnras/staa3891](https://doi.org/10.1093/mnras/staa3891)

DES Collaboration, Abbott, T. M. C., Acevedo, M., et al. 2024, *ApJL*, 973, L14, doi: [10.3847/2041-8213/ad6f9f](https://doi.org/10.3847/2041-8213/ad6f9f)

DESI Collaboration, Abdul-Karim, M., Aguilar, J., et al. 2025, arXiv e-prints, arXiv:2503.14738, doi: [10.48550/arXiv.2503.14738](https://doi.org/10.48550/arXiv.2503.14738)

Dhawan, S., Mortsell, E., Johansson, J., et al. 2024, arXiv e-prints, arXiv:2406.01434, doi: [10.48550/arXiv.2406.01434](https://doi.org/10.48550/arXiv.2406.01434)

du Mas des Bourboux, H., Rich, J., Font-Ribera, A., et al. 2020, *ApJ*, 901, 153, doi: [10.3847/1538-4357/abb085](https://doi.org/10.3847/1538-4357/abb085)

Efstathiou, G. 2025, *MNRAS*, 538, 875, doi: [10.1093/mnras/staf301](https://doi.org/10.1093/mnras/staf301)

Foley, R. J., Scolnic, D., Rest, A., et al. 2018, *MNRAS*, 475, 193, doi: [10.1093/mnras/stx3136](https://doi.org/10.1093/mnras/stx3136)

Freedman, W. L., Madore, B. F., Hoyt, T. J., et al. 2025, *ApJ*, 985, 203, doi: [10.3847/1538-4357/adce78](https://doi.org/10.3847/1538-4357/adce78)

Ganeshalingam, M., Li, W., Filippenko, A. V., et al. 2010, *ApJS*, 190, 418, doi: [10.1088/0067-0049/190/2/418](https://doi.org/10.1088/0067-0049/190/2/418)

Garnavich, P., Wood, C. M., Milne, P., et al. 2023, *ApJ*, 953, 35, doi: [10.3847/1538-4357/ace04b](https://doi.org/10.3847/1538-4357/ace04b)

Garnavich, P. M., Bonanos, A. Z., Krisciunas, K., et al. 2004, *ApJ*, 613, 1120, doi: [10.1086/422986](https://doi.org/10.1086/422986)

Gelman, A., & Rubin, D. B. 1992, *Statistical Science*, 7, 457, doi: [10.1214/ss/1177011136](https://doi.org/10.1214/ss/1177011136)

Ginolin, M., Rigault, M., Smith, M., et al. 2025a, *A&A*, 695, A140, doi: [10.1051/0004-6361/202450378](https://doi.org/10.1051/0004-6361/202450378)

Ginolin, M., Rigault, M., Copin, Y., et al. 2025b, *A&A*, 694, A4, doi: [10.1051/0004-6361/202450943](https://doi.org/10.1051/0004-6361/202450943)

Guy, J., Astier, P., Baumont, S., et al. 2007, *A&A*, 466, 11, doi: [10.1051/0004-6361:20066930](https://doi.org/10.1051/0004-6361:20066930)

Guy, J., Sullivan, M., Conley, A., et al. 2010, *A&A*, 523, A7, doi: [10.1051/0004-6361/201014468](https://doi.org/10.1051/0004-6361/201014468)

Hallgren, L., Wojtak, R., Hjorth, J., & Steinhardt, C. L. 2025, arXiv e-prints, arXiv:2505.22216, doi: [10.48550/arXiv.2505.22216](https://doi.org/10.48550/arXiv.2505.22216)

Hamuy, M., Trager, S. C., Pinto, P. A., et al. 2000, *AJ*, 120, 1479, doi: [10.1086/301527](https://doi.org/10.1086/301527)

Hand, J., Kim, A. G., Aldering, G., et al. 2025, *ApJ*, 982, 110, doi: [10.3847/1538-4357/ad9f32](https://doi.org/10.3847/1538-4357/ad9f32)

Hatano, K., Branch, D., & Deaton, J. 1998, *ApJ*, 502, 177, doi: [10.1086/305903](https://doi.org/10.1086/305903)

Hoeflich, P., & Khokhlov, A. 1996, *ApJ*, 457, 500, doi: [10.1086/176748](https://doi.org/10.1086/176748)

Holtzman, J. A., Marriner, J., Kessler, R., et al. 2008, *AJ*, 136, 2306, doi: [10.1088/0004-6256/136/6/2306](https://doi.org/10.1088/0004-6256/136/6/2306)

Hou, J., Sánchez, A. G., Ross, A. J., et al. 2021, *MNRAS*, 500, 1201, doi: [10.1093/mnras/staa3234](https://doi.org/10.1093/mnras/staa3234)

Howell, D. A. 2001, *ApJL*, 554, L193, doi: [10.1086/321702](https://doi.org/10.1086/321702)

Hoyt, T., et al. 2026

Hoyt, T., et al. in prep.

Hoyt, T. J., Jang, I. S., Freedman, W. L., et al. 2025, arXiv e-prints, arXiv:2503.11769, doi: [10.48550/arXiv.2503.11769](https://doi.org/10.48550/arXiv.2503.11769)

Hunter, J. D. 2007, Computing in Science & Engineering, 9, 90, doi: [10.1109/MCSE.2007.55](https://doi.org/10.1109/MCSE.2007.55)

Jones, E., Oliphant, T., Peterson, P., et al. 2001, arXiv:1907.10121

Kenworthy, W. D., Jones, D. O., Dai, M., et al. 2021, ApJ, 923, 265, doi: [10.3847/1538-4357/ac30d8](https://doi.org/10.3847/1538-4357/ac30d8)

Kenworthy, W. D., Goobar, A., Jones, D. O., et al. 2025, A&A, 697, A125, doi: [10.1051/0004-6361/202452578](https://doi.org/10.1051/0004-6361/202452578)

Kessler, R., Becker, A. C., Cinabro, D., et al. 2009, ApJS, 185, 32, doi: [10.1088/0067-0049/185/1/32](https://doi.org/10.1088/0067-0049/185/1/32)

Kessler, R., Guy, J., Marriner, J., et al. 2013, ApJ, 764, 48, doi: [10.1088/0004-637X/764/1/48](https://doi.org/10.1088/0004-637X/764/1/48)

Larison, C., Jha, S. W., Kwok, L. A., & Camacho-Neves, Y. 2024, ApJ, 961, 185, doi: [10.3847/1538-4357/ad0e0f](https://doi.org/10.3847/1538-4357/ad0e0f)

Lewis, A., & Challinor, A. 2011, CAMB: Code for Anisotropies in the Microwave Background, Astrophysics Source Code Library, record ascl:1102.026. <http://ascl.net/1102.026>

Maccoun, R., & Perlmutter, S. 2015, Nature, 526, 187, doi: [10.1038/526187a](https://doi.org/10.1038/526187a)

Madhavacheril, M. S., Qu, F. J., Sherwin, B. D., et al. 2024, ApJ, 962, 113, doi: [10.3847/1538-4357/acff5f](https://doi.org/10.3847/1538-4357/acff5f)

Maguire, K., Sullivan, M., Patat, F., et al. 2013, MNRAS, 436, 222, doi: [10.1093/mnras/stt1586](https://doi.org/10.1093/mnras/stt1586)

Mandel, K. S., Thorp, S., Narayan, G., Friedman, A. S., & Avelino, A. 2022, MNRAS, 510, 3939, doi: [10.1093/mnras/stab3496](https://doi.org/10.1093/mnras/stab3496)

Neveux, R., Burtin, E., de Mattia, A., et al. 2020, MNRAS, 499, 210, doi: [10.1093/mnras/staa2780](https://doi.org/10.1093/mnras/staa2780)

Newman, M. J. B., Larison, C., Jha, S. W., et al. 2025, arXiv e-prints, arXiv:2508.20023, doi: [10.48550/arXiv.2508.20023](https://doi.org/10.48550/arXiv.2508.20023)

Nicolas, N., Rigault, M., Copin, Y., et al. 2021, A&A, 649, A74, doi: [10.1051/0004-6361/202038447](https://doi.org/10.1051/0004-6361/202038447)

Ó Colgáin, E., & Sheikh-Jabbari, M. M. 2025, MNRAS, 542, L24, doi: [10.1093/mnrasl/slaf042](https://doi.org/10.1093/mnrasl/slaf042)

Perlmutter, S., Gabi, S., Goldhaber, G., et al. 1997a, ApJ, 483, 565, doi: [10.1086/304265](https://doi.org/10.1086/304265)

Perlmutter, S., Aldering, G., Goldhaber, G., et al. 1999, ApJ, 517, 565, doi: [10.1086/307221](https://doi.org/10.1086/307221)

Perlmutter, S. A., Deustua, S., Gabi, S., et al. 1997b, in NATO Advanced Study Institute (ASI) Series C, Vol. 486, Thermonuclear Supernovae, ed. P. Ruiz-Lapuente, R. Canal, & J. Isern, 749, doi: [10.1007/978-94-011-5710-0_46](https://doi.org/10.1007/978-94-011-5710-0_46)

Phillips, M. M. 1993, ApJL, 413, L105, doi: [10.1086/186970](https://doi.org/10.1086/186970)

Phillips, M. M., Lira, P., Suntzeff, N. B., et al. 1999, AJ, 118, 1766, doi: [10.1086/301032](https://doi.org/10.1086/301032)

Pinto, P. A., & Eastman, R. G. 2000, ApJ, 530, 744, doi: [10.1086/308376](https://doi.org/10.1086/308376)

Planck Collaboration, Aghanim, N., Akrami, Y., et al. 2020, A&A, 641, A6, doi: [10.1051/0004-6361/201833910](https://doi.org/10.1051/0004-6361/201833910)

Popovic, B., Brout, D., Kessler, R., & Scolnic, D. 2023, ApJ, 945, 84, doi: [10.3847/1538-4357/aca273](https://doi.org/10.3847/1538-4357/aca273)

Popovic, B., Kenworthy, W. D., Ginolini, M., et al. 2025a, arXiv e-prints, arXiv:2506.05471, doi: [10.48550/arXiv.2506.05471](https://doi.org/10.48550/arXiv.2506.05471)

Popovic, B., Shah, P., Kenworthy, W. D., et al. 2025b, arXiv e-prints, arXiv:2511.07517, doi: [10.48550/arXiv.2511.07517](https://doi.org/10.48550/arXiv.2511.07517)

Pskovskii, I. P. 1977, Soviet Ast., 21, 675

Raichoor, A., de Mattia, A., Ross, A. J., et al. 2021, MNRAS, 500, 3254, doi: [10.1093/mnras/staa3336](https://doi.org/10.1093/mnras/staa3336)

Riddell, A., Hartikainen, A., Lee, D., et al. 2018, stan-dev/pystan: v2.18.0.0, v2.18.0.0, Zenodo, doi: [10.5281/zenodo.1456206](https://doi.org/10.5281/zenodo.1456206)

Riess, A. G., Press, W. H., & Kirshner, R. P. 1996, ApJ, 473, 88, doi: [10.1086/178129](https://doi.org/10.1086/178129)

Riess, A. G., Filippenko, A. V., Challis, P., et al. 1998, AJ, 116, 1009, doi: [10.1086/300499](https://doi.org/10.1086/300499)

Riess, A. G., Rodney, S. A., Scolnic, D. M., et al. 2018, ApJ, 853, 126, doi: [10.3847/1538-4357/aaa5a9](https://doi.org/10.3847/1538-4357/aaa5a9)

Riess, A. G., Breuval, L., Yuan, W., et al. 2022, ApJ, 938, 36, doi: [10.3847/1538-4357/ac8f24](https://doi.org/10.3847/1538-4357/ac8f24)

Rigault, M., Copin, Y., Aldering, G., et al. 2013, A&A, 560, A66, doi: [10.1051/0004-6361/201322104](https://doi.org/10.1051/0004-6361/201322104)

Rosenberg, E., Gratton, S., & Efstathiou, G. 2022, MNRAS, 517, 4620, doi: [10.1093/mnras/stac2744](https://doi.org/10.1093/mnras/stac2744)

Ross, A. J., Samushia, L., Howlett, C., et al. 2015, MNRAS, 449, 835, doi: [10.1093/mnras/stv154](https://doi.org/10.1093/mnras/stv154)

Rubin, D., Aldering, G., Barbary, K., et al. 2015, ApJ, 813, 137, doi: [10.1088/0004-637X/813/2/137](https://doi.org/10.1088/0004-637X/813/2/137)

Rubin, D., Aldering, G., Betoule, M., et al. 2025, ApJ, 986, 231, doi: [10.3847/1538-4357/adc0a5](https://doi.org/10.3847/1538-4357/adc0a5)

Savage, B. D., & Mathis, J. S. 1979, ARA&A, 17, 73, doi: [10.1146/annurev.aa.17.090179.000445](https://doi.org/10.1146/annurev.aa.17.090179.000445)

Scalzo, R., Aldering, G., Antilogus, P., et al. 2014, MNRAS, 440, 1498, doi: [10.1093/mnras/stu350](https://doi.org/10.1093/mnras/stu350)

Scolnic, D., Rest, A., Riess, A., et al. 2014, ApJ, 795, 45, doi: [10.1088/0004-637X/795/1/45](https://doi.org/10.1088/0004-637X/795/1/45)

Senzel, R., Maguire, K., Burgaz, U., et al. 2025, A&A, 694, A14, doi: [10.1051/0004-6361/202451239](https://doi.org/10.1051/0004-6361/202451239)

Smith, M., Sullivan, M., Wiseman, P., et al. 2020, MNRAS, 494, 4426, doi: [10.1093/mnras/staa946](https://doi.org/10.1093/mnras/staa946)

Sullivan, M., Le Borgne, D., Pritchett, C. J., et al. 2006, ApJ, 648, 868, doi: [10.1086/506137](https://doi.org/10.1086/506137)

Sullivan, M., Conley, A., Howell, D. A., et al. 2010, MNRAS, 406, 782, doi: [10.1111/j.1365-2966.2010.16731.x](https://doi.org/10.1111/j.1365-2966.2010.16731.x)

Taylor, G., Jones, D. O., Popovic, B., et al. 2023, MNRAS, 520, 5209, doi: [10.1093/mnras/stad320](https://doi.org/10.1093/mnras/stad320)

Torrado, J., & Lewis, A. 2021, JCAP, 2021, 057, doi: [10.1088/1475-7516/2021/05/057](https://doi.org/10.1088/1475-7516/2021/05/057)

Tripp, R. 1997, A&A, 325, 871
—. 1998, A&A, 331, 815

Tristram, M., Banday, A. J., Górski, K. M., et al. 2021, A&A, 647, A128, doi: [10.1051/0004-6361/202039585](https://doi.org/10.1051/0004-6361/202039585)

Tristram, M., Banday, A. J., Douspis, M., et al. 2024, A&A, 682, A37, doi: [10.1051/0004-6361/202348015](https://doi.org/10.1051/0004-6361/202348015)

Tucker, M. A. 2025, MNRAS, 538, L1, doi: [10.1093/mnrasl/slae121](https://doi.org/10.1093/mnrasl/slae121)

van der Walt, S., Colbert, S. C., & Varoquaux, G. 2011, CSE, 13, 22, doi: [10.1109/MCSE.2011.37](https://doi.org/10.1109/MCSE.2011.37)

Vincenzi, M., Brout, D., Armstrong, P., et al. 2024, ApJ, 975, 86, doi: [10.3847/1538-4357/ad5e6c](https://doi.org/10.3847/1538-4357/ad5e6c)

Vincenzi, M., Kessler, R., Shah, P., et al. 2025, MNRAS, 541, 2585, doi: [10.1093/mnras/staf943](https://doi.org/10.1093/mnras/staf943)

Wang, L., Strovink, M., Conley, A., et al. 2006, ApJ, 641, 50, doi: [10.1086/500422](https://doi.org/10.1086/500422)

Wiseman, P., Sullivan, M., Smith, M., et al. 2021, MNRAS, 506, 3330, doi: [10.1093/mnras/stab1943](https://doi.org/10.1093/mnras/stab1943)

Wojtak, R., & Hjorth, J. 2025, arXiv e-prints, arXiv:2506.22150, doi: [10.48550/arXiv.2506.22150](https://doi.org/10.48550/arXiv.2506.22150)

Wojtak, R., Hjorth, J., & Hjortlund, J. O. 2023, MNRAS, 525, 5187, doi: [10.1093/mnras/stad2590](https://doi.org/10.1093/mnras/stad2590)